NuSTAR, *Swift*, and *NICER* observations of Cen X–3

Philipp Thalhammer

15.11.2019

Dr. Karl Remeis Sternwarte Bamberg

Friedrich-Alexander-Universität Erlangen-Nürnberg

Supervisor: Prof. Dr. Jörn Wilms

Contents

1 Abstract **3**

2 Introduction **4**

3 Formation of Accretion neutron stars **4**
3.1 Stellar Evolution & Formation of Neutron Stars 4
3.2 Formation of High mass X–ray binaries 5

4 Physics of Accreting Neutron Stars **5**
4.1 Accretion in X-Ray Binaries 5
4.2 Spectral formation in the Accretion column 8
4.2.1 X-Ray Continuum 8
4.2.2 Phenomenological models 11
4.2.3 Cyclotron lines (CRSF) 12

5 Satellites **14**
5.1 Swift 14
5.2 Suzaku 15
5.3 NuSTAR 16
5.4 NICER 17
5.4.1 Mission Objective 19
5.4.2 Mission Design 20
5.4.3 Backgrounf Estimation 22

6 *NICER* observation of the 2019 outburst of 4U 1901+03 **25**

7 Cen X–3 **28**
7.1 NuSTAR & Swift observation of Cen X–3 28
7.1.1 Observation & Data Reduction 29
7.1.2 Fitting the accretion rate of `BWsim` (Methodology) 29
7.1.3 Results 31
7.1.4 The MCMC hammer 34
7.1.5 Discussion 35
7.2 NICER observation of Cen X–3 38
7.2.1 Observation & Data Reduction 38
7.2.2 Results 39

8 Conclusion & Outlook **44**

1 Abstract

Neutron stars are the collapsed cores of massive stars after they underwent a supernova explosion. This collapse vastly amplifies their density, magnetic field and speed of rotation, leading to one of the most extreme environments in the universe. In binary systems featuring neutrons stars, matter can be transferred from the companion onto the neutron stars surface. The strong magnetic field in the order of 10^{12} G forces the infalling material to follow the magnetic field lines and to impact onto the magnetic poles of the neutron star. At the poles the stream of matter is decelerated and the kinetic energy is released in the form of X-rays. As the magnetic dipole axis generally is not aligned with the axis of rotating, the X-ray flux of these sources appears pulsed with the rotation period. Studying the radiation escaping the extreme environment around these accreting X-ray pulsars can provide unique insights about the limits for our current physical theories. Currently there are ∼350 known accreting pulsar. The first source that could be identified as such by its pulsed X-ray emission is Cen X–3. As such this source is well studied. This thesis will discuss new data of Cen X–3 taken by the *NuSTAR* and *NICER* satellites. *NICER* is still a very "young" X-ray detector installed on board the ISS in June 2017. As a consequence, there are still many unknowns concerning its calibration and background modelling. Much of the work that went into this thesis went into understand those.

Another less studied source is 4U 1901+03. It orbits a massive Be star and exhibits semi-regular outburst every 10-20 years. The most recent outburst took place in early 2019 and was monitored with *NICER* with a total exposure time of ∼ 100 ks. Part of thesis was concerned with the data extraction for this data set. A detailed analysis including additional *NuSTAR* data will be presented by Coley et al. (in prep.). A quick look at the data, however, already reveals a strong correlation between spectral hardness and X-ray luminosity and a constant pulse profile, which implies accretion in the sub-critical regime without a significant change in the accretion geometry.

For Cen X–3, first, the spectral data taken by *NuSTAR* and *Swift*, covering a wide energy range, is modelled. This was done with classical phenomenological models as well as with the physical accretion column model *BWsim* by Becker & Wolff (2007). For the application of *BWsim*, a new approach for the fitting procedure is implemented, which simplifies its application considerably. The resulting phenomenological fits agree well previous result, while there are significant deviations to previous "by eye" fits concerning the physical model. More recent, more rigorous fits, on the other hand, seem to converge on similar parameters. While the new approach solves one issue of *BWsim*, it is stressed that the complexity of the parameters space still introduces systematic uncertainties, which have to be treated with care.

To further study the spectral evolution over the binary orbit of Cen X–3, data taken with *NICER* was used. It covered about 1.5 orbital periods, including two eclipses. While the exposure time in each point was limited, the data clearly showed the drastic spectral changes during the occultation of the neutron star. While the unobscured spectrum fits well to the previous observations taken in this state, during dips in luminosity pulsation ceases and fluorescence lines of helium-like Ne, Mg, Si, S and highly ionized iron becomes visible. Looking at the pulsation of these line and their flux over the binary orbit, their different region of origin could be constrained.

2 Introduction

People have always been drawn to the extreme conditions found in nature. Whether it was the cold of the Antarctic, the pressure of the Mariana Trench or the violent heat of a volcano. These environments show us the strangeness of our wold and most importantly, at-least for the physicist, they enable us to test the limits of our current understanding of the universe. When looking for extreme conditions among the natural sciences, one in inevitably drawn towards astrophysics. And one of the most extreme environments even in astrophysics can probably be found in and around neutron stars. These collapsed stellar cores comprise more than a solar mass within a dense ball the size of a medium sized city such as Munich. They feature the strongest stable magnetic and gravitational fields found outside of black holes. Some of these objects are born in binary systems, accreting matter from a ordinary main sequence stars. The radiation emitted by these system usually reaches X-rays energies and the can become one of the brightest objects in the galaxy at these energies. Studying the accretion and spectral formation in these systems will be the topic of the following thesis.

3 Formation of Accretion neutron stars

To understand the properties and population of X-ray binaries it is essential to understand their formation. This section will give a brief overview of how these compact object and especially neutron star are formed and how they behave in binary systems.

3.1 Stellar Evolution & Formation of Neutron Stars

Following There are basically two ways a neutron star can form. As a product of Type Ib or II supernova or when a white dwarf accretes matter and collapses into a neutron star Saio & Nomoto (1985); Ruiter et al. (2019); Janka (2012).

The first case starts with an heavy main sequence star with a Zero Age Main Sequence (ZAMS) mass at-least $7\,M_\odot$ (Smartt, 2009). Although the relationship between the end stage of a stars stellar evolution depending and its mass and composition is this only poorly understood (Sukhbold et al., 2016).

The following description is based on Janka (2012) and Sukhbold et al. (2016), which can be referred to for for details. During their save life on the main sequence these stars continue to burn hydrogen in their center, creating a growing helium core. When the stellar core becomes hot enough, helium fusion stars rapidly though out the core and the star transitions in the red giant phase. From that point onward the stars burns though heavier and heavier elements in ever shortening time periods, continuously leading to hotter and denser core. Still can continue as long as the is some pressure to hold the core up against gravity. When temperature and pressure become high enough electron capture and photodissociation begins to deprive the core of the energy and electron, initializing the collapse. Electron capture during the collapse leads to an increasing neutonalization of the core, eventually forming a proto-neutron star. When most of the electron and protons have been converted into neutron the core becomes supported by neutron degenerate

pressure and becomes almost in-compressible. As this contraction and hardening takes place in a matter of seconds the outer shells are stilling onto the proto-NS surface and just "bounce off". This starts a outwards moving shock wave. This shock wave, however, is soon stalled by the infalling material. The stalled shock is than accelerated outwards by the deposition of energy behind the shock by the intense neutrino radiation released by the contraction core. This outwards moving shock than disrupts the star leading to the supernova. What is left is the expanding shell of the supernova remnant and the newly formed neutron star. For heavy star it can happen that not all of the outer shells can escape the gravitational well of the NS and material falls back onto the NS. This additional material can push the NS over the Oppenheimer-Volkov limit, causing it to collapse to a black hole.

The second formation channel begins with a lower mass star in a binary system collapsing to a white dwarf. Either the binary companion is a main sequence star or already another white dwarf. In case of a MS star, it can transfer mass to the WD via accretion. As the WD gains mass it will eventually exceed the Candrasekar mass limit and collapse. For WDs consisting mainly out of oxygen this will ignite fusion of carbon to heavier elements and the released energy will disrupt the WD. This would be a Type Ia supernova. For oxygen neon WDs it is possible that electron capture sets in before the disruption. This process converts electrons and protons to neutrons and let energy escape in form of neutrino. The reduced temperature and electron density allows the WD to further contract and eventually for a neutron Star just as in the case of the isolated supernova(Saio & Nomoto, 1985). In a binary system of two WDs it is that they can shed their angular momentum via gravitational radiation and collide. It is expected that these collisions are able to produce NSs (Gvaramadze et al., 2019).

Strong evidence for the existence formation of NSs from white dwarf is the large population of young millisecond pulsars in otherwise old stellar clusters where no recent supernova could have happened. These neutron stars show combination of fast spin, high spin-down rate and strong magnetic field that is expected from newly formed neutron stars. This discrepancy could be explained if a significant portion of neutron stars are form from older white dwarfs (Tauris et al., 2013).

3.2 Formation of High mass X–ray binaries

4 Physics of Accreting Neutron Stars

4.1 Accretion in X-Ray Binaries

X-ray binaries are fueled by the release of gravitational potential energy during the accretion of matter from the optical companion onto the compact object. A more detailed description of accretion mechanisms in astrophysics can be found in the books this overview is based on, namely Longair (2011) and Frank et al. (2002). Accretion onto a compact object is one of the most efficient ways to release energy in nature. As such it drives the luminous processes in the universe. Generally the potential energy can be released via accretion of matter with the mass m onto an

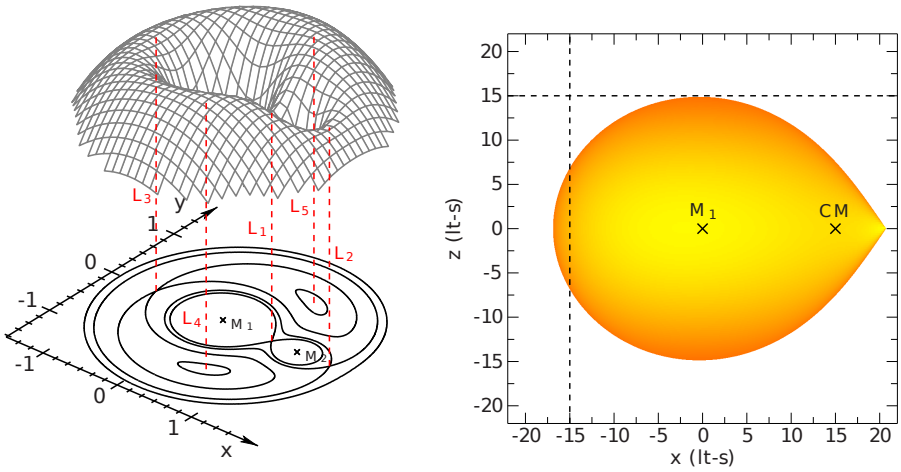

Figure 1: Left: Roche Potential for $M_1/M_2 = 0.8$. The red, dotted lines indicate the positions of the five Lagrangian points. Right: Surface of a donor star filling its Roche lobe. CM marks the position of the center of mass. Taken from Bissinger (2016).

object with the mass M and the radius R is given by

$$\Delta E = \frac{GMm}{R}, \tag{1}$$

where G is the Gravitational constant. For a typical neutron star this turns out to be $\sim 0.1 c^2$. Assuming that this energy escapes in the form of radiation, this implies a luminosity of

$$L = \frac{GM\dot{m}}{R}, \tag{2}$$

where $\dot{m}$ is the rate of accretion. Therefore, an accretion rate of $\sim 10^{18} gs^{-1}$ or $1.6 M_{odot}/yr$ are required to fuel the X-ray immensities usually seen in bright pulsars such es Cen X–3, Her X-1 or LMC X–4 (Becker & Wolff, 2007). In the following it will be discuss how such an amount of matter can be transfer from the optical companion onto the neutron star.

The mass transfer from the donors can be divided into the following three main mechanisms: Roche-Lobe overflow, Stellar winds and Be-Disk.

Roche-Lobe overflow occurs in close binaries when the surface of on the stars exceeds its Roche Lobe. The Roche Lobe describes the region close to each star in which co-rotating matter is still bound to its star. Further away centrifugal forces and the gravitational pull of the companion enables matter to cross the potential barrier at the Lagrange point L_1 (see Fig 1). The combined Roche potential $\Phi(\vec{r})$ is given by

$$\Phi(\vec{r}) = -\frac{M_1 G}{|\vec{r} - \vec{r}_1|} - \frac{M_2 G}{|\vec{r} - \vec{r}_2|} - \frac{1}{2}(\vec{\Omega} \times \vec{r})^2, \tag{3}$$

where M_i and $\vec{r}_i$ are the two masses and position vectors, G is the gravitational constant and $\vec{\Omega}$ is the angular momentum. If the surface of one star reaches to the L_1 point mass can be transferred

to the Roche Lobe of the companion. Due to the conservation of angular momentum, this leads to the formation of an accretion disk around the smaller counterpart. A well studied example would be Her X-1 (e.g., Schandl & Meyer, 1994). Viscous friction, shocks or inelastic scattering can transfer angular momentum from the faster rotation inner regions of the accretion disk outwards. This enables material to fall closer towards the neutron star and drives a disk wind at the disk edges. As material moves toward the neutron star it reaches a point, at which the ram pressure of the gas will be overcome by the magnetic field pressure. The radius at which this happens is called the Alfvén radius $r_{\rm mag}$ and is given by

$$r_{\rm A} = \left(\frac{8\pi^2}{G}\right)^{1/7} \left(\frac{R^{12} B_{\rm p}^4}{M\dot{M}^2}\right)^{1/7} = 1800{\rm km} \left(\frac{R}{10{\rm km}}\right)^{12/7} \left(\frac{B}{10^{12}{\rm G}}\right)^{4/7} \left(\frac{M}{1.4M_\odot}\right)^{-1/7} \left(\frac{\dot{M}}{10^{-7}M_\odot{\rm yr}^{-1}}\right)^{-2/7} \tag{4}$$

, where R,B,M and $\dot{M}$ are the radius, magnetic field, mass and accretion rate of the neutron star. Inside this radius matter is forces onto to follow the magnetic field lines until it reaches the neutron star. From this condition and assuming a simple dipole to estimate the radius of the hot spot and the accretion column at the neutron star surface can be estimated to by

$$r_0 \lesssim R_* \left(\frac{R_*}{r_{\rm A}}\right)^{1/2} \tag{5}$$

For further details see, e.g., Lamb et al. (1973),Ghosh & Lamb (1979) and Harding et al. (1984).

Stellar winds become the dominant form of mass transfer around massive OB-type companions. These stars exhibit mass loss rates$\sim 10^{-7} - -10^{-5} M_\odot\,{\rm yr}^{-1}$ and reach terminal velocities $\sim 1000 - -3000\,{\rm km\,s}^{-1}$ (Conti & McCray, 1980).

The interaction between the radiation from the optical star and the X-rays from the compact companion with the stellar wind leads to a complicated wind structure that strongly deviated from a spherical geometry leading to complex spectral changes on various timescales.

Photoelectric absorption of soft X-rays by the stellar can significantly influence the X-ray spectrum of the companion. This is especially significant close to an eclipse then the radiation passes close to the massive star. An example for an wind accreting system would be Vela X-1 or Cyg X-1 (Sako et al., 1999; Hirsch et al., 2019). The stellar wind in these system only carries little angular momentum and is, therefore, unlikely to form an accretion disk around the neutron star (Petterson, 1978). Its geometry will be more symmetrical, leading to quasi-spherical accretion, often described as Bondi-Hoyle accretion (Bondi & Hoyle, 1944; Bondi, 1952).

Be-Stars are rapidly rotating massive stars of type B. At the equator material is fast enough to be ejected and forms a circumstellar disk. In the stellar spectrum the disk becomes visible though additional hydrogen emission lines and often an excess in infrared emission. In binary systems the compact companion can pass though the Be-Desk close or at periastron leading to regularly repeating outbursts. These outburst are referred to as Type-I outbursts. Additionally there are irregular giant outburst of Type-II. These can happen at any orbital phase and are believed to be caused by changes in the donor star such as instabilities in the Be-disk (Martin et al., 2014). During the pariastron passage material can be accreted, e.g., via Roche-Lobe overflow forming a

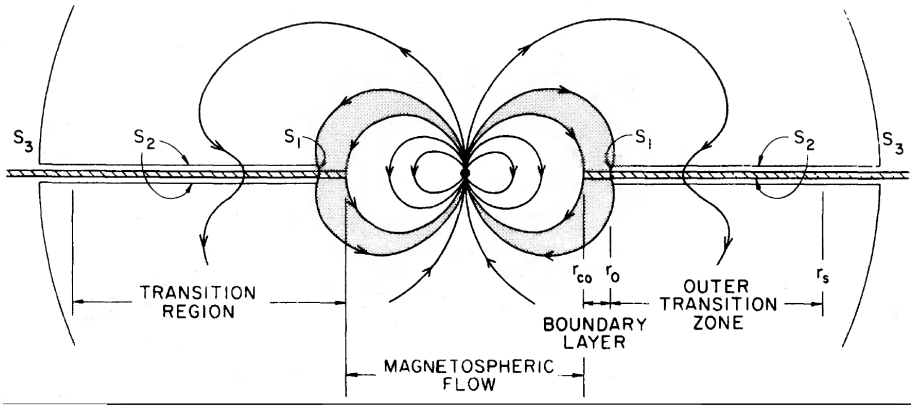

Figure 2: Geometry aof the accretion disk and the magnetic field around an accretion neutron star. Taken from Ghosh & Lamb (1979). Look there for a detailed discussion of the involved radii.

accretion disk, which might persist even outside of periatron (D'Angelo & Spruit, 2012).

- Cen X-3 has accretion disk so write a few sentences about loosing angular momentum.
- Describe coupling to the magnetic field and Alfeen radius
- Estimation of the polar radius from Alfeen radius and dipole geometry

4.2 Spectral formation in the Accretion column

When material reaches the neutron star magnetosphere, its motion will be dominated by the magnetic field of the neutron star. It will follow the magnetic field lines and is funneled into a columnar geometry above the magnetic poles. Here the material decelerates and the kinetic energy is released in form of X-rays. The mechanism through which the material is slowed down strongly depends on the magnetic field strength and the accretion rate. A detailed discussion of different accretion regimes can be found in Becker et al. (2012) and therein.

The accretion flow reaches velocities of ∼0.6 c before the matter reaches the radiation-dominated shock. For typical luminosities of $L_X \sim 10^{37--38}\,\mathrm{erg\,s^{-1}}$ the shock can rich a high of several kilometers. By passing though the shock region the flow velocity is reduced by a factor of ∼7. After the shock the flow has to decelerate to come to a rest on the NS surface. This can happen via two different modes: By the pressure from the radiation field or by coulomb interaction. The transition from Coulomb to radiation decelerated takes places when the luminosity exceeds the critical luminosity

$$L_{\mathrm{crit}} \approx 1.5 \times 10^{37} B_{12}^{16/15} \mathrm{erg\,s^{-1}}, \tag{6}$$

where B_{12} is the surface magnetic field in term of 10^{12} G Becker et al. (2012).

4.2.1 X-Ray Continuum

Calculating the spectra that emerges from such a magnetized plasma has been a challenge for many years. Early calculations to solve the radiative transfer and calculate the emerging spectra, were

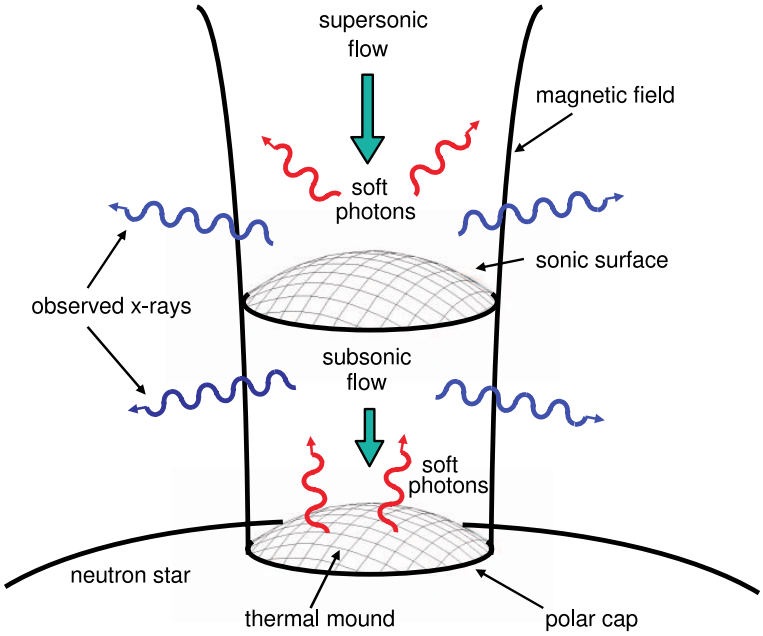

Figure 3: Accretion geometry in assumed by BW07. The infalling supersonic matter forms a standing shock and ungoes inverse Compton scattering with soft seed photons (red). The so produced high-energy X-rays (blue) escape through the side of the column in a fan-beam pattern. Taken from Becker & Wolff (2007).

unable to reliably describe the observed data (Meszaros & Nagel, 1985a,b; Nagel, 1981a,b; Klein et al. 1996). The following description of the spectral formation is based on the work by Becker & Wolff (2007) (hereafter BW07), who focus on the high luminosity case ,where the stream of matter is decelerated by the gradient in the radiation pressure.

In their model the gas enters the cylindrical column through the top, passes through a extended radiation-dominated standing shock region and reaches the thermal mould with a velocity of zero. The geometry is illustrated in Fig. 3

To make the the radiative transport equation separable in energy and space and therefore able to be solved analytically, a velocity profile proportional to the optical depth is assumed. For the radiative transport equation they account for both bulk and thermal Comptonization of seed photons (i.e. first- and second-order Fermi energization due to collisions with the decelerating gas). This leads a two-dimensional radiative transfer equation for the photon distribution $f(z, \epsilon)$ depending on the position z and the photon energy ϵ given by

$$\frac{\partial f}{\partial t} + v\,\frac{\partial f}{\partial z} = \frac{dv}{dz}\,\frac{\epsilon}{3}\,\frac{\partial f}{\partial \epsilon} + \frac{\partial}{\partial z}\left(\frac{c}{3 n_e \sigma_{\parallel}}\,\frac{\partial f}{\partial z}\right) - \frac{f}{t_{\rm esc}} + \frac{n_e \bar{\sigma} c}{m_e c^2}\,\frac{1}{\epsilon^2}\,\frac{\partial}{\partial \epsilon}\left[\epsilon^4\left(f + kT_e\,\frac{\partial f}{\partial \epsilon}\right)\right] + \frac{Q(z,\epsilon)}{\pi r_0^2}\ , \quad (7)$$

where z is the distance from the stellar surface along the column axis, $v < 0$ is the inflow velocity, Q denotes the photon source distribution, and $t_{\rm esc}$ represents the mean time photons spend in the plasma before diffusing through the walls of the column.

From left to right, this is what the terms mean:

- The expression on the left side of the the equation denotes the time derivation of the photon density in the comoving reference frame.
- The first term on the left side describes first-order Fermi energization ("bulk Comptonization") in side the radiative shock region and as such depends on the deceleration of the gas flow dv/dz. The corresponding velocity profile is shown in Fig 2 and Eq 29 & 30 in BW07.
- The second term, resembling Fick's equations, describes the diffusion of photons along the the vertical column axis.
- The rate of escape of photons though the column walls is determined the the escape time t_{esc}. An expression for the $t_{\rm esc}$ is given by Eq. 66 in BW07. The escape time along the column height will also influence from which part of the accretion column most of the photons will escape.
- Thermal Comptonization can be understood as inverse Compton scattering with the randomly moving electron and is described by the Kompaneets operator (Kompaneets, 1957). This operator also describes the recoil of electrons and thus the transfer of energy from high to low photon energies. While, generally bulk Comptonization will be dominant, the Kompaneets operator is therefore still crucial to account for the observed high energy cut-off.
- The last term accounts for the injection of seed photons into the accretion column. There populations of seed photons are by BW07.
  - Cyclotron Radiation: As is discussed further in section 4.2.3, the strong magnetic field lead to the formation of discrete Landau levels in electrons spiralling around the magnetic field lines. Excitation of these collisions happens predominately via collisions with protons. Due to their short life-time, however, collisional deexitations is completely negligible. Instead, the deexitation generates photons with energies around the the cyclotron energy. Broardening by the thermal motion of electrons and by the magnetic field gradient along the column axis is neglected as it is assumed to be masked by Comptonization. Therefore, he source term is defined as monochromatic and distributed throughout the column.
  - Blackbody Radiation: The hot thermal mould at the bottom of the accretion column forms another source of seed photons. This blackbody emission is distributed in frequency according to Planck's law but localized to the height of the thermal mould. BW07 showed, that for many pulsars the blackbody radiation contributes only very little to the population of seed photons. It is however the term which takes by far the most computation time to calculate. For an initial fit it is therefore often practical to deactivate the blackbody contribution.
  - Bremsstrahlung Radiation: This term describes the spectrum due to Bremsstrahlung radiation by the electrons streaming along the magnetic field (free-free emission). As this term is extended in energy as well as in space its analytical its analytical solution is the most complex (see E1. 128 in BW07).

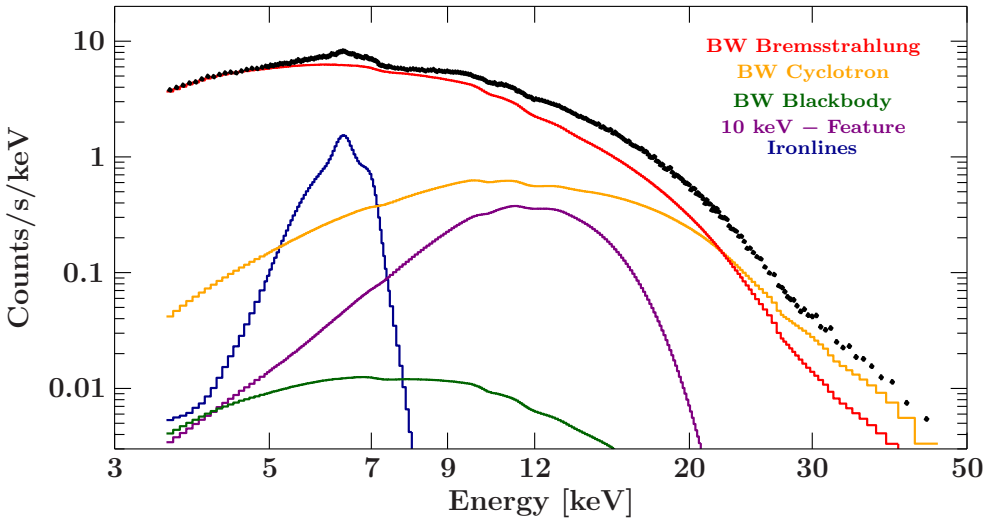

Figure 4: Application of BW07 to *NuSTAR* data of Cen X–3 showing the different model components including an iron line complex and a "10 keV-Feature" which unfortunately is still often required.

To be able to solve the transfer equation analytically, BW07 assume that the accretion flow with an approximate velocity profile , in a steady state and consisting of a fully ionized hydrogen plasma. Furthermore, a cylindrical symmetry, a constant B-field and temperature along the column is assumed. The electron cross-sections, are only calculated for electrons propagating parallel or perpendicular to the magnetic field only for the mean photon energy. These assumptions have to be kept in mind when interpreting specific fitting result. An example fit, showing the different source terms is shown in Fig 4.

Some of the assumption made by BW07, such as the a cylindrical symmetry, constant B-field and simplified gas dynamic, could have been relaxed by newer models (West et al., 2017; Postnov et al., 2015), but so far BW07 is still unique, in the sense that it both accurate and fast enough to be fitted to actual data.

4.2.2 Phenomenological models

Traditionally the X-ray continuum originating from the accretion column is model with phenomenological models, These models generally are comprised of a power-law describing high energy emission from inverse Compton spattering. Addition all thermal Comptonization is will transfer transferring energy from high- to low-energy photons leading to an exponential cut-off at energies above 12-20 keV. There are multiple ways to implements such an exponential cut-off and one has to decide for each source which one is best used to describe the spectrum. One should keep in mind that that the choice of continuum model can have a significant impact on the parameters of additional line and absorption features, especially broader features, i.e the CRSF (Boldin et al., 2013, , Kühnel in prep.) The most common choices of cut-off models are the following:

- Cutoffpl: In this very simple model the cutoff is implemented by a single exponential factor

and is, therefore, described by a single parameter. Despite its simplicity it often sufficient, especially for data with a low SNR.

$$\texttt{cutoffpl}(E) = E^{-\alpha} \exp(-E/\beta) \tag{8}$$

- Highcut: The high-energy cut-off model only take the exponential term only into account for energies about a certain threshold E_c. As such it does not effect the powerlaw at low energies, but leads to discontinuous change in the spectral slope. This can lead to line-like feature in the residuals, which sometime have to be modeled with an additional Gaussian feature.

$$\texttt{powerlaw}(E) \times \texttt{highcut}(E) = E^{-\alpha} \begin{array}{ll} \exp\left[(E_c - E)/E_f\right] & E \geqslant E_c \\ 1.0 & E \leqslant E_c \end{array} \tag{9}$$

- Fdcut: To solve this problem the fdcut used a continuous cut-off model after the Fermi-Daric distribution (Tanaka, 1986).

$$\texttt{powerlaw}(E) \times \texttt{ fdcut } (E) = E^{-\alpha} \frac{1}{1 + \exp\left(\frac{E - E_{\rm cut}}{E_{\rm fold}}\right)} \tag{10}$$

- NPEX: If none of the models listed above can describe the continuum, the NPEX model is often used. It consists of two power-laws, one with a positive and one with a negative exponential index. Although it can lead to line-like features around the cut-off as well. (Brumback et al., 2018).

$$\texttt{NPEX}(E) = n_1 \left(E^{-\alpha_1} + n_2 E^{-\alpha_2}\right) e^{-E/kT} \tag{11}$$

4.2.3 Cyclotron lines (CRSF)

During the accretion of matter onto the poles of the neutron star the magnetic field forces the electrons to spiral around the magnetic field lines. In the classical regime the radius of these spirals is given by the Lamor radius. For magnetic fields in the order of 10^{12} G, as they are found in neutrons stars, the electrons momentum perpendicular to the magnetic field becomes quantized. Or rather the quantisation becomes measurable. It follows, that electrons can only orbit the magnetic field lines at a specific radii, leading to discreet energy levels. For a detailed description of this phenomenon see Schwarm et al. (2017) or Schönherr et al. (2007), which this section is based on. The energy of these levels are given as integer multiples of the so called cyclotron energy $\mathrm{E_{cyc}}$, which is given by the so called *12-B-12* rule

$$E_{\rm cyc} = \frac{\hbar e}{m_e c}(1+z)^{-1} B_{12}\,\mathrm{keV} = 11.6(1+z)^{-1}\,B_{12}\,\mathrm{keV}, \tag{12}$$

where $\hbar$ is the reduced Planck constant, e the elementary charge, m_e the charge of the electron, B_{12} is the magnetic field strength in the unit of $10^{12}G$ and z is the gravitational red-shift experienced by photons escaping the gravitational well of the NS. The energy levels can be exited by the

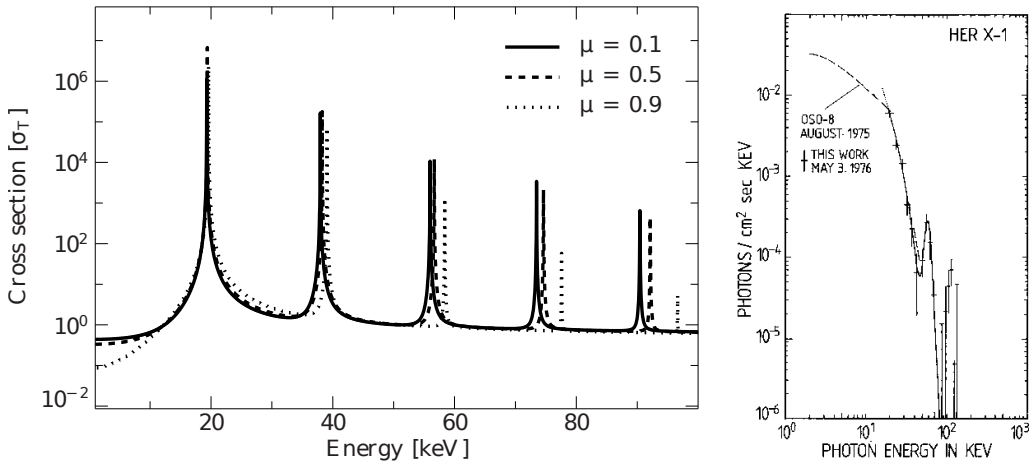

Figure 5: Left: Scattering cross section as a function of rest frame energy for electron in initial Landau level $n_i = 0$ to level n_f with $n_i \leqslant n_f \leqslant 6$ with a fundamental cyclotron resonance at ∼20 keV. The solid, dashed, and dotted lines show cross sections for different angles between photon path an the B-filed. Taken from Schwarm et al. (2017). Right: The first detected cyclotron absorption line seen by Truemper et al. (1978) in Her X-1 at at ∼58 keV.

absorption of photons with the appropriate energies, leading to an increased absorption cross-section (see Fig 5) The lifetime of higher Landau levels is very short (Latal, 1986). The electrons therefore return to the ground state almost instantaneously, leading to a scattering process.

In the outer regions of the accretion column this interaction can scatter photons out of the line of sight of the observer, leading to an absorption feature called a cyclotron resonant scattering feature (CRSF) or simply cyclotron line (Schönherr et al., 2007). The first such feature was found 1987 in Her X-1 by Truemper et al. (1978) and has since be found in many pulsars (Add some citations). The observed line energy depends on the local magnetic field strength at the line forming region. This makes the CRSF a powerful tool to directly measure the magnetic field strength inside the accretion column. The position of the line forming region depends on the position at which photons can escape the column. Consequently a change in accretion geometry and shock height can affect the observed cyclotron energy (Malacaria et al., 2015; Becker et al., 2012). As such the the evolution of the cyclotron line can with energy can be used to track changes in the accretion regime.

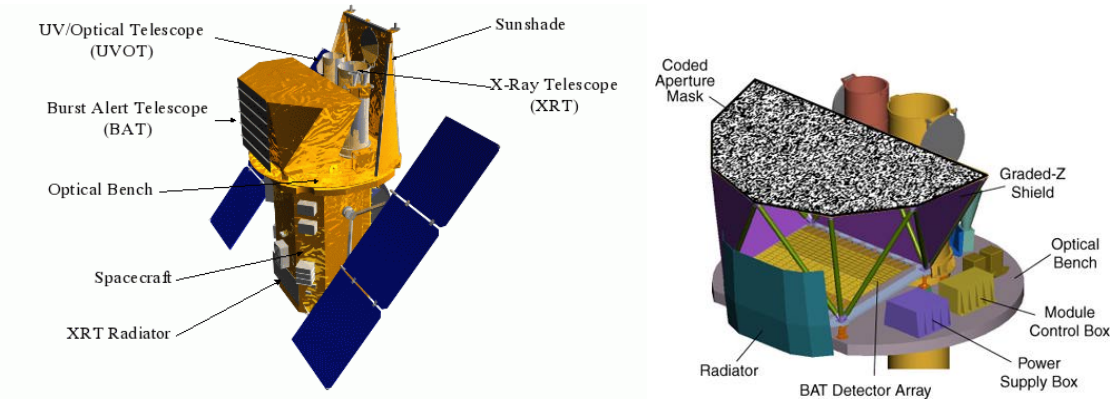

Figure 6: sketch showing the layout of the different instruments (left) and the BAT in particular (right). From `https://www.swift.ac.uk/about/instruments.php`

5 Satellites

We are currently living in a golden age of X-ray astronomy. Never before have there been so many and so powerful X-ray satellites in orbit. The ones that have been used in this work will be described in the following chapter.

5.1 Swift

The Neil Gehrels *Swift* Observatory, previously *Swift* Gamma-Ray Burst Mission, is a multi-wavelength satellite designed as part of NASA's Medium Explorers program (MIDEX) specifically to investigate gamma-ray bursts (GRBs). It was launched on 2004 November 20 on board of a Delta II rocket. Three instruments are part of the satellite: The UV/Optical Telescope (UVOT), the X-ray Telescope (XRT) and Burst Alert Telescope (BAT). A detailed description of the satellite can also be found in Gehrels et al. (2004) and Burrows et al. (2005).

For a sketch of the satellite layout see Fig 6.

The spacecraft is able to autonomously slew towards any detected GRB and to provide multi-wavelength overage of their afterglow. And With a slew rate of 50° in less than 75 s *Swift* is able to reach most detected GRBs within the first minute.

The UV/Optical Telescope (UVOT) is an optical and ultraviolet Ritchey–Chrétien telescope with a wavelength range of 170 nm – 600 nm and an 30 cm aperture. Its main purpose is to study the rapidly dimming optical afterglow of GRBs. As it was not used in this work it will be further discussed here. For a detailed description consult Roming et al. (2005).

The X-ray Telescope (XRT) is Wolter Type-I telescope with a similar design to the *Suzaku*/XIS. It covers an energy range of 0.2–10 keV and is designed to to perform follow-up observation of GRB detection by BAT. It has an angular resolution of of 18″(FWHM), a 23′ FOV and an effective area of 110 cm^2 and an energy resolution of 190 eV at 10 keV.

To be able to observe sources over a wide range in flux the CCD, which is similar to the *XMM-Newton*/MOS detector, can be read out in different modes. Standard photon-counting

mode delivers the full spectral and spacial resolution but, due to the increasing effects of pile-up, is limited to fluxes below ∼45 mCrab. In Windowed timing mode the CCD is continuously read out in one direction sacrificing information about one spacial dimension for a high time resolution of 2.2 ms and a reduced susceptibility to pile-up. For the brightest sources with fluxes between 5–27 Crab imaging mode is recommended. Here no spectroscopic measurement is , an integrated image measuring only the total energy deposited energy per pixel is recorded.

The Burst Alert Telescope (BAT) is a coded-mask telescope with a wide FOV designed to detect GRBs and perform an automatic all-sky hard x-ray survey [1]. For a detailed description of the instrument see Barthelmy et al. (2005). Its half-open coded-mask aperture consist of 54,000 randomly distributed lead elements and covers and area of 2.5 m^2. This coded-mask design enables the BAT to have a large FOV of 1.4 sr (half-coded) and 2.7 sr (partially-coded). Its 32 768 CdZnTe detectors are positioned one meter below the coded-mask covering an energy range of 15 – 150 keV. Its main objective it to detects and subsequently locate GRBs with a precision of 1″-4″. This allows the spacecraft to bring the source into the FOV of *SWIFT*s two other instruments. Simultaneously *Swift*/BAT performs an all-sky survey, generation light curves for over 1000 sources (Krimm et al., 2006). The standard light curves available as part of it its survey are limited to the 15 keV–50 keV band.

5.2 Suzaku

Astro-E2, later renamed *Suzaku*, was the successor to the failed X-ray mission Astro-E which was lost on 2000 February 10 during launch (Mitsuda et al., 2007). Five years later *Suzaku* was launched successfully on board the the M-V launch vehicle. Installed on board the satellite were three instruments: The X-Ray Imaging Spectrometer (XIS), the Hard X-Ray Detector (HXD) and the X-Ray Spectrometer (XRS). As sketch of the satellite is shown in Fig 7.

The XRS (Kelley et al., 2007) was the first X-ray microcalorimeter on any X-ray satellite and had an excellent energy resolution of 6–7 eV. Unfortunately it failed shortly after the launch as its liquid Helium cooling failed.

The XIS (Koyama et al., 2007) consisted of four detector modules (XIS0–3) each with its own Wolter-Type I X-Ray Telecope (XRT) focusing the X-ray onto the detectors. The four detectors were CDD detectors similar to those previously used for the *Chandra*/ACIS and *XMM-Newton*/EPIC detectors. They had a energy range of 0.2-12 keV with an energy resolution of 130ėV at 6 keV. It had a field of view of 17.8′×17.8′. Additionally to the normal CCD read-out, the XIS detectors could be read out "burst" mode, "Window" mode and "timing" mode. Burst mode restricted the read-out in time by introducing an artificially dead time during each frame, reducing the effects of pile-up. Window mode spatially restricts the read-out to only parts of the CCD. In Timing mode the pulse height from 128 rows were summed together into a single row along the Y direction. In this mode charge transfer happened continuously, sacrificing one image dimension for a better timing resolution of 7.8 ms. For the normal read-out mode the timing resolution was 8 s and decreased with the read-out fraction in Burst and Window mode. One of the four detectors

[1] `https://swift.gsfc.nasa.gov/results/transients/`

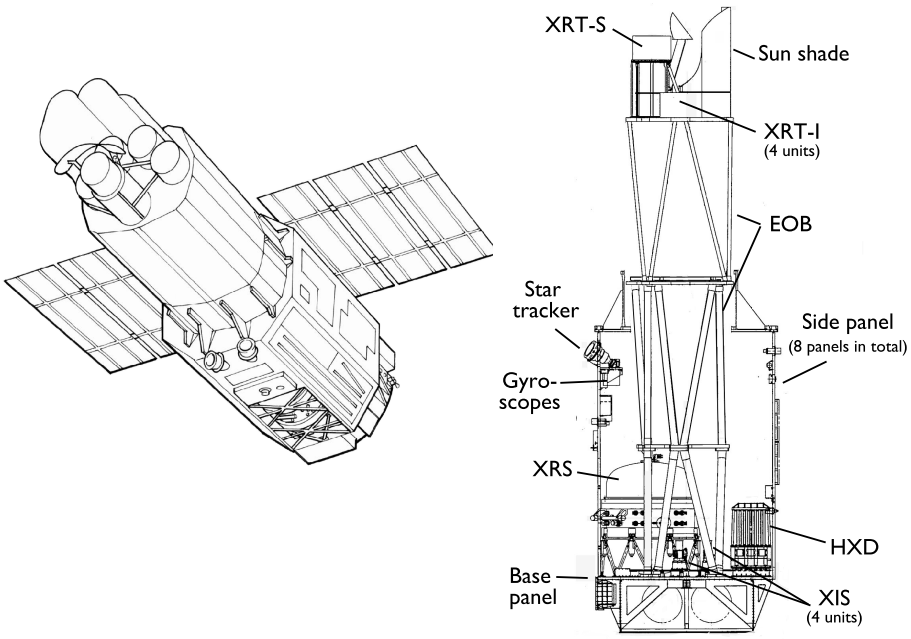

Figure 7: Sketch of the satellite exterior (left) and inner layout, indicating the position of the different instruments. (Mitsuda et al., 2007)

(XIS1) was back-illuminated. The other three front illuminated. As the back-illuminated detector was more sensitive at low energies and the front-illuminated ones a high energies, this led to a slightly wider usable energy range. The total effective area of the XIS is shown in Fig. 8.

The third main instrument was the Hard X-ray Detector (HXD)(Takahashi et al., 2007). It used a X-ray collimator to expend *Suzaku*'s sensitivity from 10 keV to 600 keV band. Its detectors consisted of 16 main detectors and are surrounded by 20 crystal scintillators, which provide active shielding. Each main detector was composed of two parts: The PIN Silicon diode array (PIN) and the GSO/BGO phoswich counter (GSO). The first being sensitive to energies between ∼10 keV and 70 keV and the latter up to ∼600 keV. The energy resolution (FWHM) of the PIN detector is ∼3.0 keV and $7.6/\sqrt{E}\%$ for the scintillators.

In 2006, XIS2 was hit by a micro-meteorite, leaving it unusable [2].After 10 years of successful scientific operation, *Suzaku* completed its mission in 2015 and was permanently switched off.

5.3 NuSTAR

NuSTAR is a high energy X-ray satellite launched in 13 June 2012. As it is a Small Explorer mission, it had to fit in the low-cost, air-launched Pagasus XL rocket. It consists of two identical co-aligned grazing incidence telescopes, each sensitive to photons with energies between 3 keV and 79keV. *NuSTAR* was the first mission using Wolter Type-I optics to provide imaging capabilities at such high energies. Until then coded mask technology was used for such applications, though

[2] `http://www.astro.isas.jaxa.jp/suzaku/news/2006/1123/`

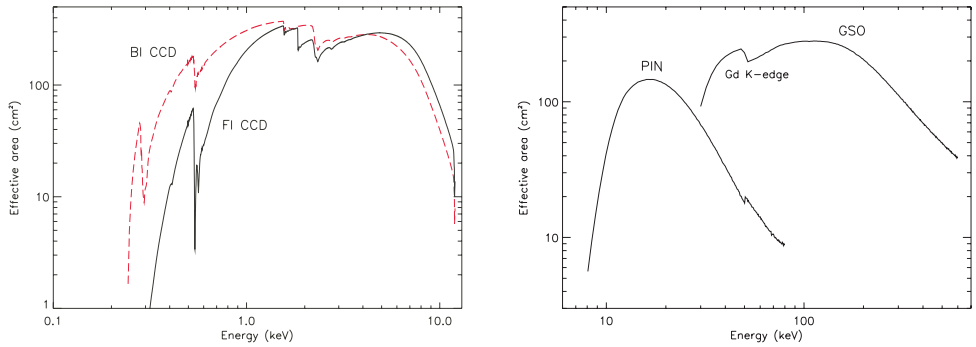

Figure 8: Effective area of the single XIS detectors (left) and the PIN and GSO detectors (right). Note the difference between the front- and back-illuminated XIS detectors (Mitsuda et al., 2007)

this generally leads to worse resolution and efficiency. It has been paced on a nearly circular, low inclination orbit at a height of around 600 km. This orbits allows almost continuous ground contact. enabling quick reaction times to ToOs and its low inclinations minimizes interference due to the SAA. To be able to focus X-rays with energies above 10 keV *NuSTAR* need to have a very low reflection angle for its mirror modules. From that follows a long focal length of 10.4 m. This is much more than would fit into the 2 m long fairing of the Pagasus XL rocket. This has been solved by placing an extendable mast between focal plane and mirror modules. This mast, however, is not stiff enough to ensure a constant focal point on the X-ray detectors. Due to thermal expansion and during slewing of the space craft the mast can deform and move the focused spot on the detector by about a millimeter. To reconstruct each photon direction an aspect/metrology system is used. It consists of four star trackers (three on the spacecraft bus and one on the optic bench) plus two laser metrology units. The mirrors themselves each consist of 133 nested multilayer-coated grazing incidence shells in conical approximation to a Wolter-I geometry. Their multilayer coating is essential to increase sensitivity at high energies. The two sets of X-ray detectors are solid state CdZnTe pixel detectors surrounded by CsI anti-correlation shields. Each detector consists of a 2x2 array each in turn consisting of 32x32 pixels. The resulting overall effective are is shown in Fig 9. *NuSTAR*'s high sensitivity at high energy makes it uniquely suited for studying CSRFs in accretion neutrons stars. Its time resolution relative to the on board time is 2 μs. The energy resolution is 400 eV at 10 keV and thus about a factor of two worse than what can be achieved with SDDs and CCDs e.g. of Suzaku-XIS or the *NICER*-XRT.

5.4 NICER

In 2017 a new mission X-ray telescope joint the growing zoo of X-ray missions. On June 3 the *Neutron Star Interior Composition Explorer* (NICER) was launched on board of an Falcon 9 rocket as part of SpX-11, the twelfth ISS resupply mission performed by SpaceX. As *NICER* is still new and a central focus of this thesis its description more indepth than for the other used instruments. There are a few aspects that set *NICER* apart from other recent X-ray mission. The most apparent is its position on board the ISS (see Fig. 11) and consequently lower costs. The other aspect is its clearly defined mission goal, which is already reflected in its name.

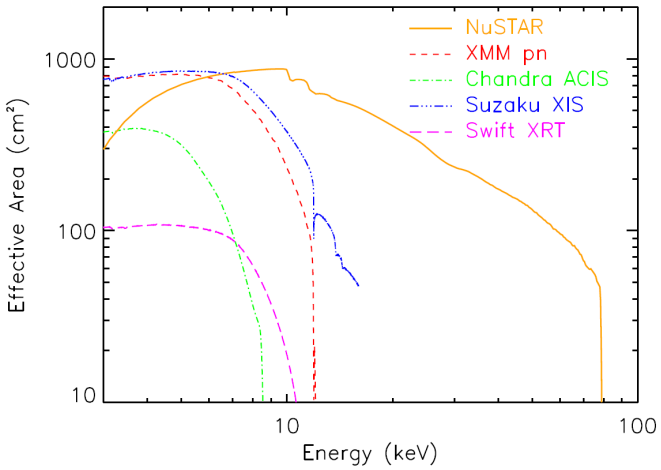

Figure 9: Comparison of the total effective area of *NuSTAR*, *XMM-Newton* and *Suzaku* (Harrison et al., 2013)

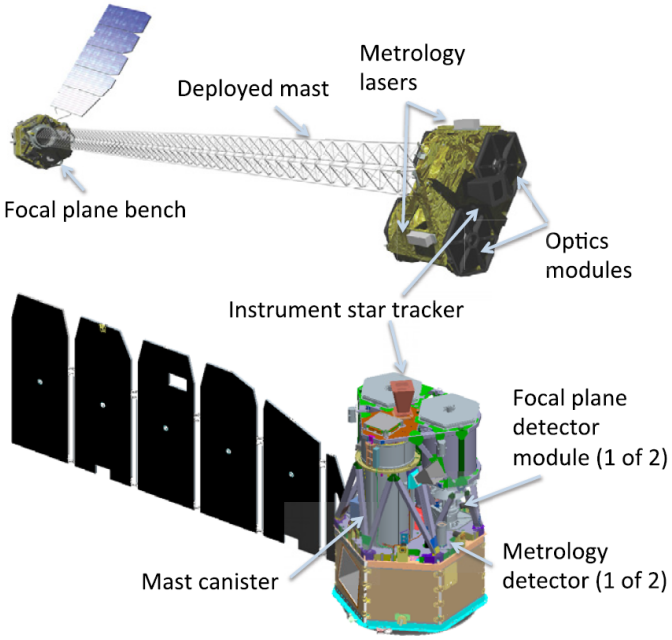

Figure 10: Diagram showing *NuSTAR* in its fully deployed state (top) and s sketch of its design before mast deployment as it is stored during launch (bottom)

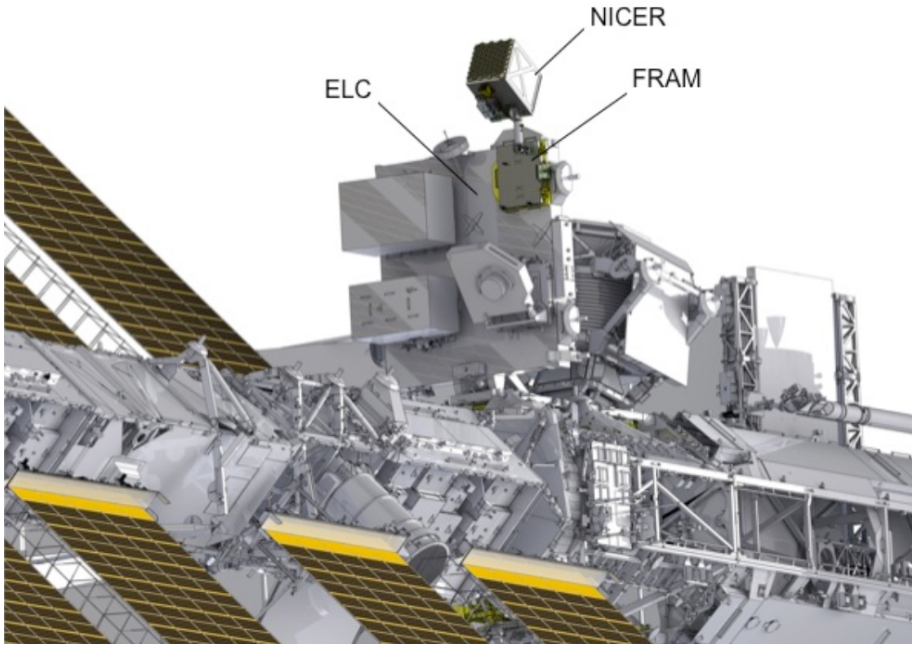

Figure 11: *NICER* as it is positioned on board the ISS (Gendreau et al., 2012)

5.4.1 Mission Objective

While a lot as been learned about the physics in the environment around neutron stars in the recent years, this can not be said about the composition of their interior. Its small size and high opacity makes it challenging to perform any measurement of the NSs interior. With densities several times higher than inside a atomic nucleus, the exact state of the neutron star matter depends on basic unknowns of nuclear physics, such as the incompressibility of bulk nuclear matter, the three-body interaction potential, and the density-dependent nuclear symmetry energy. To constraint these unknowns, *NICER* was developed as part of NASA's Explorers Program. Each possible description of the neutron star interior leads to a certain, so called, equation of state (EOS). It describes how the radius of a neutron star depends on its mass. As the composition of neutron stars interior is still unknown, so is their equation of state. To distinguish between different EOSs NICER focuses on measuring NS mass and especially radii to unprecedented precision with an uncertainty of 5-10%. This makes it possible to place each measured pulsar in a M-R diagram (see Fig. 12). Their position can then be compared with the possible mass radius tracks allowed by different theoretical models. Those theories, unable to account for the measured parameter combination can thereby be ruled out. To be able to measure the radius of a neutron star so such a precision *NICER* is looking at rotation-powered neutron as their environment is less influenced by accretion making their X–ray emission more predictable. *NICER* will focus on pulsars which produce X–rays primarily via thermal emission at their two hot-spot. AS their emission profile

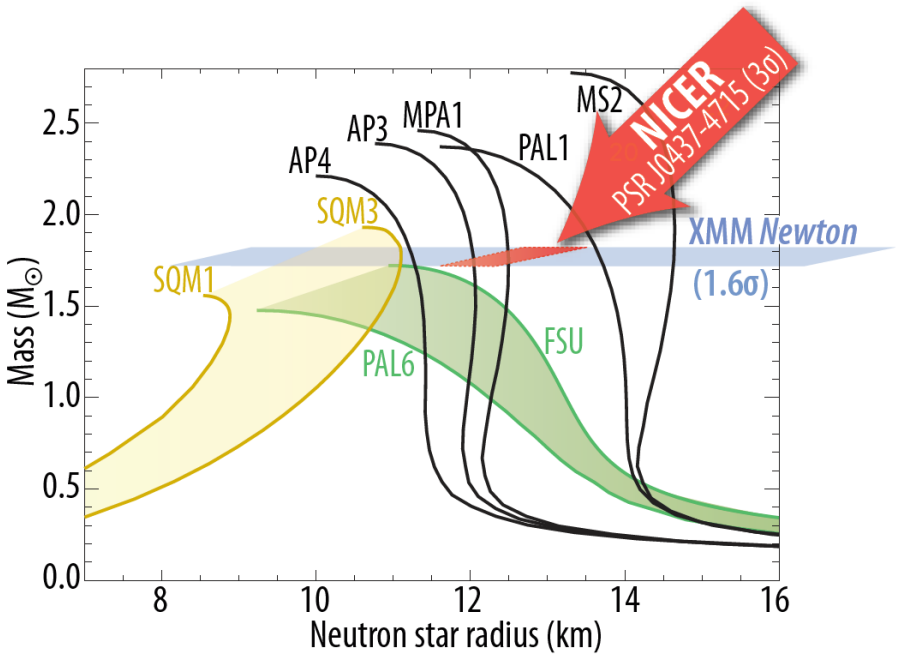

Figure 12: Mass radius diagram showing the radius and mass estimates possible with *NICER* and *XMM-Newton* for PSR J0437–4715. The plotted EOS tracks also show how these measurements can distinguish between different proposed models. (Gendreau et al., 2012)

over the NS rotation period is sensitive to mass and radius, this makes it possible to constrain both to necessary precision. Prigozhin et al. (2016)

5.4.2 Mission Design

While most other telescope are parts of dedicated satellites, NICER on the other hand took advantage of the possibility to mount a telescope on the exterior of the International Space Station. This way, *NICER* is able take full advantage of the existing infrastructures supplied by the Station's ExPRESS Logistics Carriers (ELCs). This includes power supply, high bandwidth up- and down-link, telemetry and high precision GPS connection. This ultimately leads to significantly reduced cost and risk for the mission.

So be able to perform pulse resolved studies with the necessary SNR *NICER* needs a larger collecting area. This is achieved by 56 separate mirror modules each with their own silicon drift detector (SDD). The mirrors are X–ray concentrates (XRCs) similar to those used for *Hitomi* and *Suzaku* (see Fig. 13. These mirrors use Wolter I grazing incidence optics to focus the X–rays onto the detectors. Usually Wolter optics consist of two mirrors. One parabolic one to focus the light rays and on hyperbolic one to correct for the inherit come of the parabolic mirror. As *NICER* is only designed to look at on-axis point sources, imaging capability is not required. The only reason for the mirrors is provide a smaller field of view and to focus the light on smaller detectors. Both minimises noise and background contamination. For that reason *NICER* uses only parabolic mirrors, which helps to reduce costs, weight and increases efficiency as fewer photons

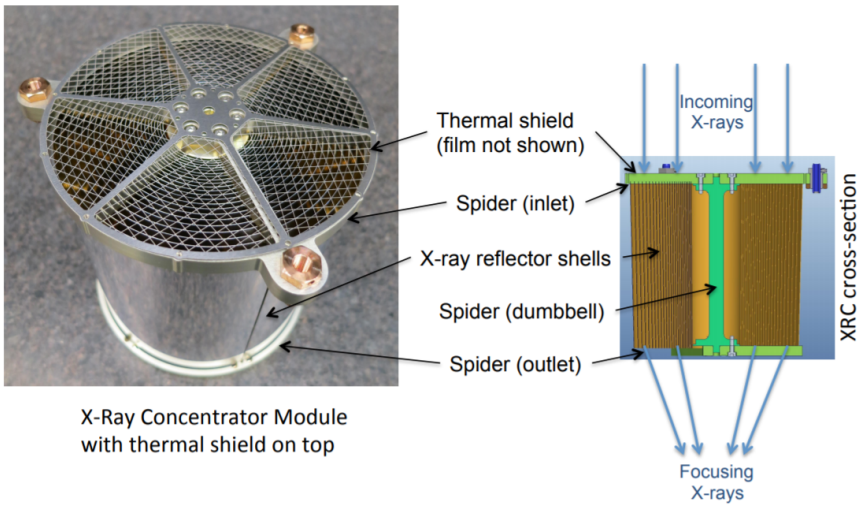

Figure 13: Image of the 56 XRCs on the left and a sketch of the XRC mirror structure on the right (Okajima et al., 2016)

are lost during the second reflection. Each XRC consists of 24 mirror shells and has a diameter of 10.5 cm. The focal length of 1.085 m enables are compact design. Usually Wolter foil optics use a flat conical approximation to the parabolic shape of the mirror. This simplifies the production and introduces only minor broadening of the point spread function. For the small focal length of *NICER* this approach is less viable, as it would significantly impact the x–ray concentration. The engineering team at the NASA Goddard Space Flight Center had to go though the additional struggle of manufacturing the curved mirror shape. This improvement increased the flux on the 2 mm aperture of the SSDs by 190 %. (Okajima et al., 2016; Balsamo et al., 2016)

Each XRC focuses the incoming photons onto a single SDD. The 56 detectors are manufactures by Amtek and organized a 7×8 array structure. The key characteristics are a low background a high timing resolution. To minimize the background, specifically the dark current, the detectors are cooled to -55° by are thermoelectric cooler. Usually SDD are would not be ideal for timing sensitive measurements, as variable drift time to the central read-out anode leads to an inherit uncertainty in the measured photon arrival times. This can be mitigated by minimizing the size of the detector. Therefore *NICER* only uses detectors with a size of 25 mm^2 and an additional aperture is installed on top of the detector, to illuminate only the central 2 mm. This reduced the timing uncertainty introduced by the SDD and the detector electronics to an acceptable value of about 70 ns. An additional advantage of the added aperture is that the protected detector volume can be used as background rejection volume. The 56 detectors are grouped into eight arrays. The signal from each array is further processed by one of eight measurement and power units (MPUs). The whole electronic setup is shown in Fig. 14. In the MPUs the data processing is split into two parallel circuits. A "fast" chain, which handles the reconstruction of the arrival time and "slow" chain, which handles the reconstruction of the pulse energy. The difference between those two is the width of the respective bandpass filter. The main purpose of those filters is to suppress high

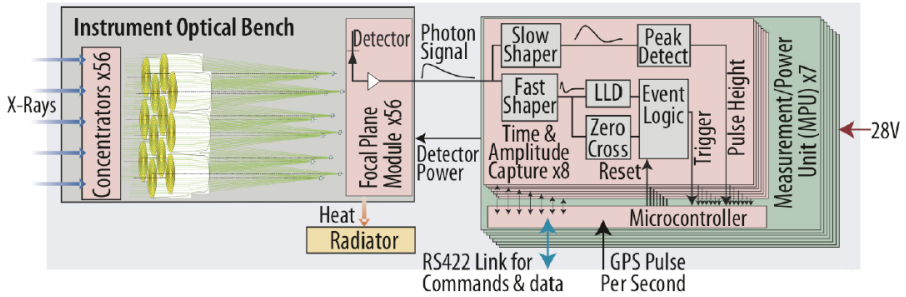

Figure 14: Sketch of the nicer electronic board including the x–ray concentrators, and the focal plane module. Arzoumanian et al. (2014)

frequency noise. As this noise affects the energy reconstruction, the slow chain has a more narrow filter. The fast chain, on the other hand, includes a much wider range of frequency components to achieve a better timing accuracy.

The two processing chains also play an important role in rejection of background events. It is possible exploit the fact that a larger distance from the detector center increases the rise time and this the detected amplitude of an event. This decrease in amplitude, however, is only significant for the fast chain, where the rise time is in the order of the peak time. Thus the ratio of fast and slow amplitude can reliably sort out events not coming from the central 2 mm region of the detector. With this setup *NICER* reaches an total effective area of 1793 cm^2 (see Fig. 15) an time resolution of < 300 nsec and an energy resolution of 137 eV at 6 keV.

Its position on the ISS, however, reduces its operations efficiency to around 33–50% and limits the duration for continuous observation. Still, in the first 18 months *NICER* is expected to reach the 10 Msec necessary to achieve its primary mission goals (Prigozhin et al., 2016).

5.4.3 Backgrounf Estimation

As *NICER* lacks imaging capabilities, it is not possible to estimate the background spectrum from a source-free region on the detector. It the therefore required to model the background. For *NICER* tools to generate such modeled background spectra for each observation are still very much work-in-progress. Generally there are two types of background generators currently available. One is based on exterior parameters during the observation, such as the orientation of the spacecraft, position in earth magnetosphere and the space weather. The other one is based on an analysis of the detected events. Both kind of models try to categorize an observation depending on the respective set of parameters. It is then possible to generate a background file from a similar "category" from a large background library. This library has bee generated over the first observation period and consists of many megaseconds of exposure on background fields that have already been used by RXTE (Jahoda et al., 2006).

Both estimator tools have recently been made public and can be download from the *NICER* webpage[3].

[3] `https://heasarc.gsfc.nasa.gov/docs/nicer/tools/nicer_bkg_est_tools.html`

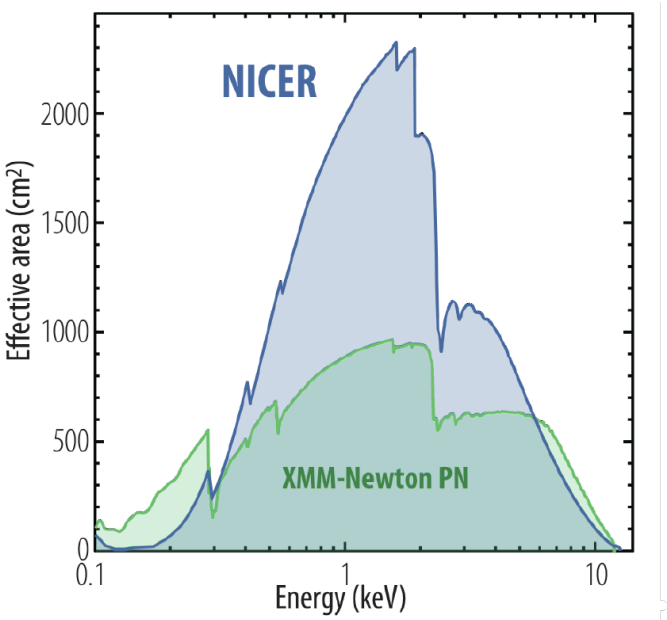

Figure 15: Comparison of the total effective area of *NICER* and *XMM-Newton* (Gendreau et al., 2012)

The tool based on exterior parameters is the `nicer_bkg_estimator` (Gendreau et al., in prep.). The three parameters used in this model to described the observation are

- The current state of the space weather, described by the the planetary Kennziffer (KP) Index (Bartels et al., 1939). KP is derived from a multiple magnetometers around the world and the us updated every 3 hours, which is a problem for local or short period changes. It ranges from 0 to 9, where low values indicate low activity, while higher indicate geomagnetic storms.
- The magnetic cut-off rigidity (COR_SAX) describes the local strength of the magnetic field. It is described by a map based on models of the International Geomagnetic Reference Field (Thébault et al., 2015).
- The angle between the current pointing and the sun. Stray light from the sun can induce significant optical loading, which can easily dominate the background at low energies. Not accounted for are, however, reflections from other objects around the ISS.

These there parameters are generally good enough to reproduce the background to reasonable accuracy in most cases. However, as the used background tool is still in development, the `nicer_bkg_estimator` fails under certain conditions, e.g., when there are no reference observations in its library.

The second tool, based in the observed counts, is `nibackgen3C50` (Remillard et al, in prep.). It parameterizes each observation three different count rate ("3C").

- *IBG*: This component includes all events with energies from 15–17 keV. Here there effective area of the mirror drop off and only very few source events should remain. IBG should therefore be sensitive to particle background during the observation.

- *HREJ*: All events in region of 3–18 keV and orientating further away from the detector center, which is determined by the PI ration from the fast and the slow read out chain, are in include in this count rate.
- *NZ*: This includes events with an energy be low 0.2 keV and, therefore, includes low-energy noise.

Additionally the estimator distinguished between day and night observations. In both models three parameters are generally enough to reproduce the background to reasonable accuracy. However in some cases certain conditions can still lead to significant deviation. More sophisticated models incorporating both sets of criteria and even machine learning are currently in development.

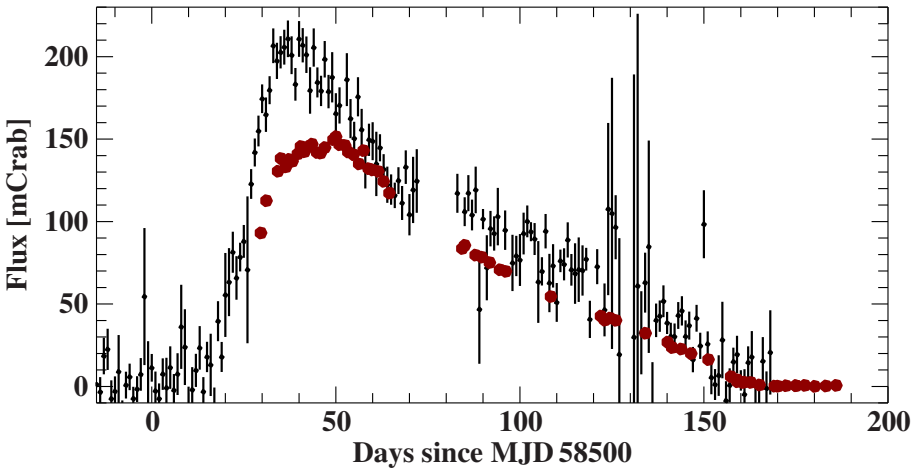

Figure 16: Lightcurve in of 4U 1901+03 during the outburst on 2019. In red the 0.5–10 keV flux detected by *NICER* and in black the 15-50 keV flux detected by *Swift*/BAT

6 *NICER* observation of the 2019 outburst of 4U 1901+03

In February 2019 the binary pulsar 4U 1901+03 went into outburst for the fourth time since 1970. 4U 1901+03 is part of a class of Be X-ray binary transients which exhibits outburst on timescales as long as 20 years and have long orbital periods with low eccentricities. As there is no obvious way to circularize such a wide orbit, these systems challenge the assumption that binary NSs are generally born with a strong natal kick and thus eccentricity. The source was first detected by the *Uhuru* satellite during an outburst in 1970 (Forman et al., 1976). It stayed visible for at least 120 days and reach an . Afterwards it was undetected until February on 2003 when it underwent a giant outburst and was visible for about five month (Reig & Milonaki, 2016). This outburst reached a luminosity of $\approx$ 240 mCrab and lasted 150 days. Most of the outburst was observed by *RXTE*. However, the limited angular resolution did not allow for a reliable identification of the optical companion. Reig & Milonaki (2016) reported on transitions trough multiple accretion regimes during this outburst and hint for the existence of a luminosity dependent cyclotron line. However, they also emphasized the importance of additional observation with more sensitive instruments during the next outburst. The next outburst came in 2011. This one, however, only reached a luminosity of 23 mCrab and lasted only for for about a month (Sootome et al., 2011). The outburst was detected by the X-ray monitors *Fermi*/GBM, *MAXI* and *Swift*/BAT, but due to the short duration and low brightness no further observations were performed. The next and most recent time 4U 1901+03 became detectable was in February 2019.

The outburst was first detected by MAXI(ATel #12498). It lasted ~150 days and reached a peak luminosity of 150 mCrab. Shortly after the onset of the outburst *Swift*/XRT observed the source for 500 s constraining the source position to within a 90% confidence radius of 2.3″(see Atel #12514). With the refined position a possible companion candidate could be identified in the UKIDS-DR6 catalogue (Lucas et al., 2008): J190339.39+031215.6 (0.6″ offset). According to the Gaia Catalog this would place the system at a distance of 2.9 kpc (Bailer-Jones et al., 2018).

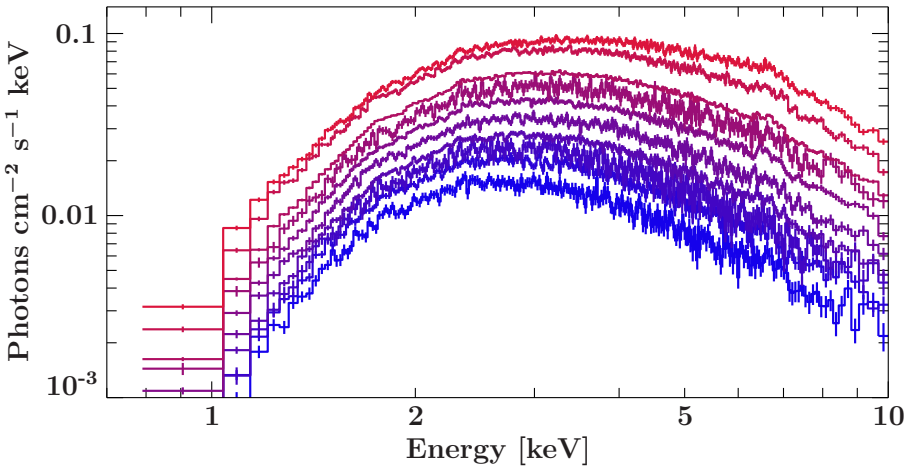

Figure 17: Spectral evolution over the course of the dimming outburst. Spectra early during the outburst are shown in red, while those later during the outburst are drawn in blue.

After it was first detected, the outburst was also regularly observed with *NICER* (see Fig. 16). To further pin down the spectral properties, especially at higher energies, four additional *NuSTAR* observation were performed throughout the outburst with a total exposure time of 96 ks.

A detailed analysis of both *NuSTAR* and *NICER* data will be presented in a forthcoming publication by Coley et al. (in preparation). Part of this thesis was the data extraction of the *NICER* observations and a quick overview over the available data will be presented in the following.

The *NICER* data extraction was performed with the NICERDAS software package distributed with HEAsoft version 6.26.1 and CALDB XTI vers. 20190516. Due to background flares induced by high energy particles, additionally to the standard filter criteria, observations with of magnetic cut-off rigidity below 1 GeV/c were omitted. Background spectra where generated using both available tools. However, the `nicer_bkg_estimator` could only generate a background for 58 out of the 61 observations.

NICER's dense coverage of the outburst with a total exposure time of over 100 ks provides an excellent chance to gain answers on the questions raised by previous observations. For a start, the evolution spectral hardness ratio can reveal changes in the spectral formation and thus the accretion regime. During the outburst 4U 1901+03 shows a clear correlation between luminosity and hardness ratio (see Fig. 18). This has already been observed in multiple sources (Reig & Milonaki, 2016; Malacaria et al., 2015). Explanations for this variability have been presented in Becker et al. (2012) and indicates no change in accretion regime. Assuming the distance of 2.9 kpc found by Gaia, 4U 1901+03 reaches a peak luminosity of $\sim 6 \times 10^3 6\,\mathrm{ergs/s}$. Following Becker et al. (2012) the critical luminosity is given by

$$L_{\mathrm{crit}} \approx 1.28 \times 10^{37}\,(E_{\mathrm{cyc}}/10\,\mathrm{keV})^{16/15}\,\mathrm{ergs}^{-1}, \tag{13}$$

where E_{cyc} is the energy of the cyclotron line. During the outburst *NuSTAR* saw an absorption feature around 30 keV (see ATel #12684). This feature is most likely a CRSF. Using this in Eq. 13

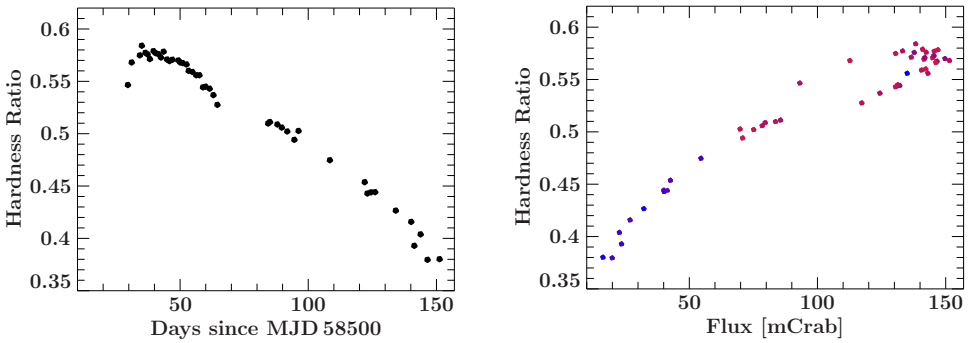

Figure 18: Left: Plot of the Hardness ratio over the course of the outburst. The Hardness ratio is calculated for flux in the energy band of 0.5–4 keV and 4–10 keV. Right: Luminosity-hardness diagram with red indicating early and blue later data points.

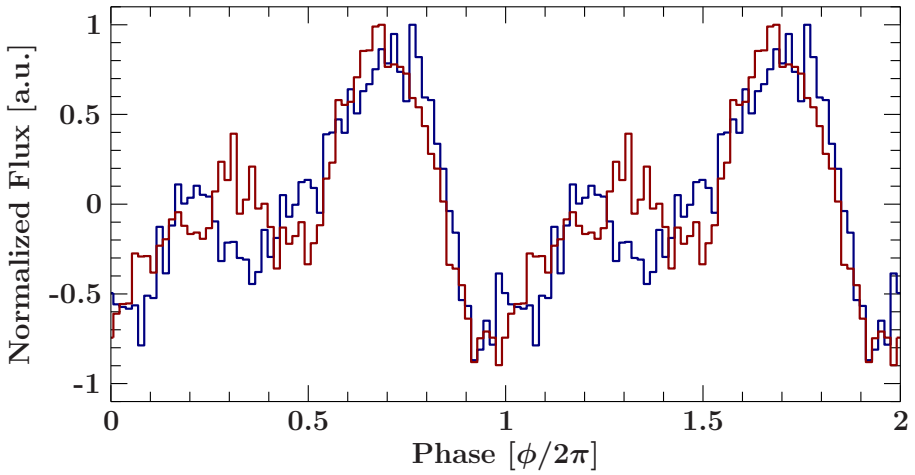

Figure 19: Comparison between the pulse profiles during the peak of the outburst (MJD 58540) and during its fading (MJD 58590).

one can derive $L_{\rm crit} \approx 4.1 \times 10^{37}{\rm ergs}^{-1}$. Therefore 4U 1901+03 probably stayed in the sub-critical regime.

Additionally to the luminosity dependence of certain spectral parameters, the pulse profile can be useful to distinguish between accretion states. Fig. 19 shows a comparison of the pulse profile during the peak and shortly after the peak of outburst, indicating no fundamental change in the accretion geometry. Although a more detailed look into the evolution of the pulse is required.

7 Cen X–3

Centaurus X-3, an accreting high mass X-ray binary (HMXB) with a spin period of ∼4.8 s and an orbital period of 2.1 d (Schreier et al., 1972). Cen X–3 was the first system which could be identiefied as an X-ray pulsar. This pulsation of its X-ray emission for first discovered in 1971 by the *UHURU* satellite (Giacconi et al., 1971). The binary system is located at a distance of 5.7 ± 1.5 kpc (Thompson & Rothschild, 2009) and consists of a neutron star with a mass of $1.2 \pm 0.2\,M_\odot$ and O 6–8 III supergiant star with a mass of $20.5 \pm 0.7\,M_\odot$ (Ash et al., 1999). The system is at high inclination, such that the neutron star (NS) is eclipsed by its donor star for around 20% of the orbital period (Suchy et al., 2008). The primary mode of mass transfer in the system happens via a Stellar wind while the the optical companion is close to filling its Roche-lobe.This leads to the formation of an relatively stable accretion disk around the NS (Tjemkes et al., 1986). Its continuum x-ray spectrum can generally be well described by a powerlaw with an exponential cut-off and a Gaussian "10-keV-feature" at around 13 keV. At ∼30 keV a CRSF was detected by (Burderi et al., 2000). Leading to an estimated local magnetic field strength of $\sim 3.5 \times 10^{12}$ G. Due to the stellar wind in the system it is often necessary to include a partial covering component to model the variable column density of the source (Naik et al., 2011). Light-curve and spectrum of Cen X–3 show variability that ranges from timescales of seconds to several days. On longer timescales, however, Cen X–3 is comparable stable and does not exhibit any outbursts (Suchy et al., 2008; Naik et al., 2011). The spectrum also features prominent iron lines of varying ionisation states at 6.4, 6.7, and 6.97 keV. Their respective intensity varies significantly with orbital phase as differently ionized clouds of material are visible. The neutral Kα neutral iron line is assumed to originate close to the neutron star surface as it is shows strong pulsation. Previous observation with *Chandra*'s grating spectrometer detected Doppler broadened Si XIII, Si XIV and Fe XXV (Iaria et al., 2005a; Wojdowski et al., 2003). Indication that these fluorescence line originate from the inner part of the accretion disk. While for the higher ionisation state, based on the line detection even during the eclipse, an origin further from the NS in the stellar wind of the companion has been proposed (Naik et al., 2011; Iaria et al., 2005b).

Over the years there have been several observations of Cen X–3, most notably in the 1970s with *UHURU*(Schreier et al., 1976), in 1989 with *GINGA* (Nagase et al., 1992), in March 1997 with *RXTE* (Suchy et al., 2008) and in December 2008 with *Suzaku* (Naik et al., 2011).

While Cen X–3 is therefore a well studied source, there has not been a detailed analysis of recent observations with *Swift*, *NuSTAR* and *NICER*, which will be the topic of the following chapter.

7.1 NuSTAR & Swift observation of Cen X–3

The following analysis of the NuSTAR & Swift observation of Cen X–3 and the the new method to retrospectively ensure energy conservation in physical models will be part of a soon to be submitted paper.

7.1.1 Observation & Data Reduction

On 2015 November 30, *NuSTAR* (Harrison et al., 2013) observed Cen X–3 with an total exposure time of 21.4 ks and 21.6 ks for the two focal plane models, FPMA and FPMB, respectively (ObsID 30101055002). These data were extracted using the official *NuSTAR* analysis software, which is part of HEASOFT 6.22 using source regions with a 120″ radius around the position of Cen X–3. Background spectra were accumulated using regions with the same radius in the southern part of *NuSTAR*'s field of view.

In order to investigate the spectrum at energies below *NuSTAR*'s lower energy cutoff data from the *Swift* X-ray (Gehrels et al., 2004) eas included. The additional data stems from an contemporaneous *Swift*-observation with ObsID 00081666001, taken on 2015-12-10 with a total exposure time of 1946 s, where 425 s were performed in Photon Counting Mode (PC) and 1522 s in Windowed Timing mode. To mitigate the significant pile up in the PC mode data, we extract data from an annulus with inner radius of 8 pixel and outer radius of 30 pixel, and use a 60 pixel circle offset from the source to measure the background. Since in Windowed Timing mode *Swift*-XRT has only 1D imaging capabilities, the central 20 pixels were used as source region and a regions between 80 pixel and 120 pixel away from the source on both sides as background.

In the following spectral analysis, which was performed with ISIS version 1.6.2-41 (Houck & Denicola, 2000), we use the *NuSTAR* data in the energy band between 3.5 keV and 79 keV, while the *Swift* data were considered in the band from 1.0 keV to 20 keV.

7.1.2 Fitting the accretion rate of `BWsim` (Methodology)

A fundamental problem with the setup of the physical model of BW07 is that it does not enforce energy conservation. In other words, the "X-ray luminosity",

$$L_{\mathrm{X}} = \int_{E_{\mathrm{min}}}^{E_{\mathrm{max}}} E * F_E(E)\, dE \tag{14}$$

where $F_E(E)$ is the model-predicted photon flux emitted in the frame of rest of the accretion column, and E_{min} and E_{max} are appropriate energy bounds, does not automatically equal the "accretion luminosity",

$$L_{\mathrm{acc}} = \frac{\dot{M} M_{\mathrm{NS}} G}{R_{\mathrm{NS}}} \tag{15}$$

where $\dot{M}$ is the mass accretion rate, M_{NS} and R_{NS} are the neutron stars mass and radius, and G is the gravitational constant. Note that both luminosities are given in the reference frame of the neutron star surface.

As discussed, e.g., by Wolff et al. (2016), when comparing the model to observations, one has to enforce energy conservation manually, by estimating $\dot{M}$ from the source spectrum. In practical terms, this is done by fitting the observed spectrum with an empirical model, i.e., some type of power-law with an exponential cut-off (see, e.g., Müller et al., 2013, for a description of the relevant models). One can use this best fit spectrum together with estimates for the object's distance as well as R_{NS} and M_{NS}, and a correction for the gravitational redshift to estimate the object's luminosity

and then derives the estimated mass accretion rate, $\dot{M}_{\rm estimate}$ from Eq. (15)[4]. This estimate is then followed by a first χ^2-minimization using a `BWsim` continuum with $\dot{M}$ held fixed at $\dot{M}_{\rm estimate}$. The resulting flux is then used to estimate a new value of $\dot{M}$, and this approach is iterated until convergence is reached in $\dot{M}$, i.e., once the relative change in $\dot{M}$ becomes smaller than a certain threshold, e.g., 1%. For the joint *Swift*/*NuSTAR* data of Cen X–3 this method converges after about 3–6 iterations.

In addition to being a very cumbersome approach that requires significant manual intervention and "baby sitting" of the fits, one issue with this iterative approach is that during each minimization step $\dot{M}$ is treated as a fixed parameter and is, therefore, not allowed to deviate from the value derived from the model luminosity. This approach neglects the fact that, e.g., the distance to the source is not precisely known, which would result in a systematic shift in the assumed accretion rate.

In order to solve this issue, a new technique which does not require an iterative approach but introduces conservation of energy directly into the data modeling, was implemented. The idea of the technique is to let $\dot{M}$ vary during the fit and to bias the fit statistics such that it disfavours values of $\dot{M}$ which do not fulfil energy conservation, i.e., for which $L_{\rm X} \neq L_{acc}$. In ISIS this approach can easily be accomplished as one has a direct programmatic access to the fit statistics calculation that allows to modify the value of the fit statistics during its minimization.

For the case of χ^2-statistics, where

$$\chi^2 = \sum_i^n (x_i - \mu_i)^2 / \sigma_i^2 \tag{16}$$

where the sum goes over all spectral channels, i, and where x_i are the data counts with uncertainties, σ_i, and μ_i the counts predicted by the model, now

$$\chi^2_{\rm final} = \chi^2 \cdot \left(1 + C \left(\frac{L_{\rm acc} - L_{\rm X}}{\Delta L_{\rm X}}\right)^{\gamma}\right), \tag{17}$$

is minimized. Here $\Delta L_{\rm X}$ is the uncertainty on the source luminosity caused be the uncertain distance to the object and other factors such as the lack of knowledge of the emission pattern and accretion column geometry, and C and γ are parameters which can be adjusted to optimize the convergence behaviour of the χ^2-minimization algorithm. Numerical experiments show that setting $C \sim 5$ and $\gamma \sim 5$ leads to quick convergence when using a Levenberg-Marquardt method.

A disadvantage of the approach is that the more complex shape of the χ^2 surface leads to a tendency of the minimization algorithm to be partly stuck in local minima. Also, away from the minima where $\chi^2_{\rm final} \neq \chi^2$ the value of $\chi^2_{\rm final}$ looses its statistical meaning. For that reason this novel approach should only be used as a tool to find a set of physical best-fit parameters and not to calculate statistical quantities, such as confidence intervals.

[4]In order to be able to equate those luminosities, it has to be assumed that the released energy is emitted isotropically, which, however, has been shown to be generally not the case (Falkner et al., 2016). Unfortunately, it is still the best guess, as the necessary information about the geometry of the system, e.g., the inclination of the neutron star's rotational axis and the emissivity pattern of the accretion columns, to improve on this assumption, is lacking

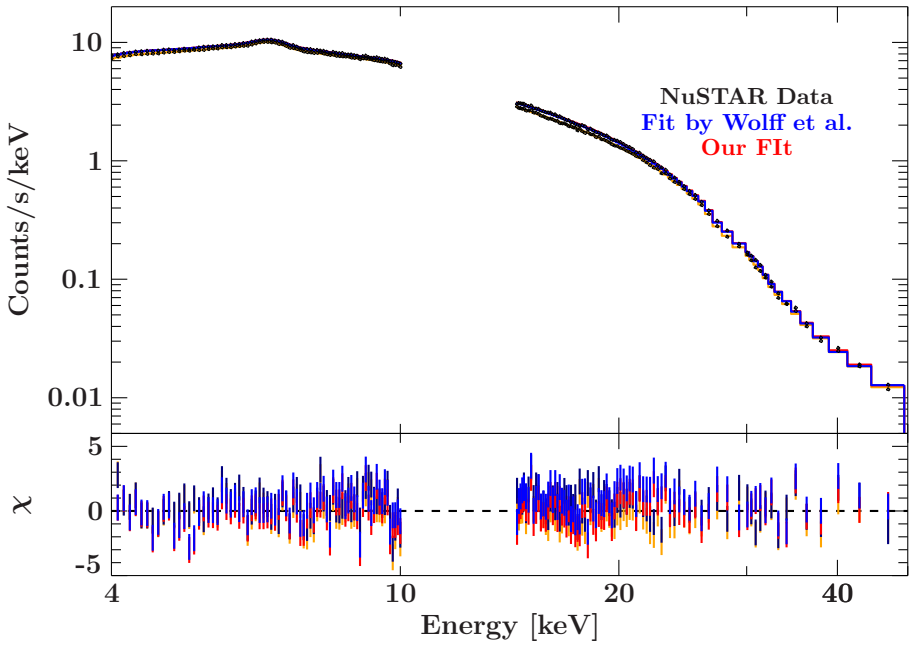

Figure 20: Comparison between the best fit to the spectrum of Her X-1, obtained with the new fitting approach (red) and the fit performed by Wolff et al. (2016) (blue)

To confirm that this new approach converges to the same results as the one used previously, it was applied to a spectrum that has already been successfully fitted with BW07. For this purpose the *NuSTAR* data of Her X-1 that has been analysed by Wolff et al. (2016) was used. Her X-1 is an intermediate-mass X-ray pulsar. It stands out for being the first source in which a cyclotron line was observed and features and precessing accretion disk with an superorbital period of 35 days (Leahy & Igna, 2012). It was observed on 2012 Septemter 22 by *NuSTAR* (ObsID 30002006005) and reached an luminosity of $\sim 4.9 \times 10^{37}\,\mathrm{erg\,s^{-1}}$. The spectrum was extracted from a 120″ region around the source and the background from a 87″ region to the the south of the FOV. The extraction was performed using Heasoft v6.22.1 and *nupipeline* v1.8.0.

Wolff et al. (2016) excluded the region between 10 and 14.4 keV due to uncertainties in the calibration, so the same was done in this analysis. The comparison between the best fit, found with the new approach, and the classical approach shown in Fig 20 clearly illustrates their convergence to equivalent fits. Any remaining deviations can be trace back to the slighly calibration used for the data extraction.

7.1.3 Results

After that reliable convergence has been confirmed, the new approach could be applied to Cen X–3. For comparison with previous works and to be able to apply the iterative approach, first the *Swift*-XRT, *NuSTAR*-FPMA, and -FPMA spectra were fitted with a phenomenological model, i.e., a powerlaw with an exponential cut-off. Bissinger et al. 2018 (in preparation) have shown that the implementation of that cut-off can have a significant influence on the cyclotron line parameters and

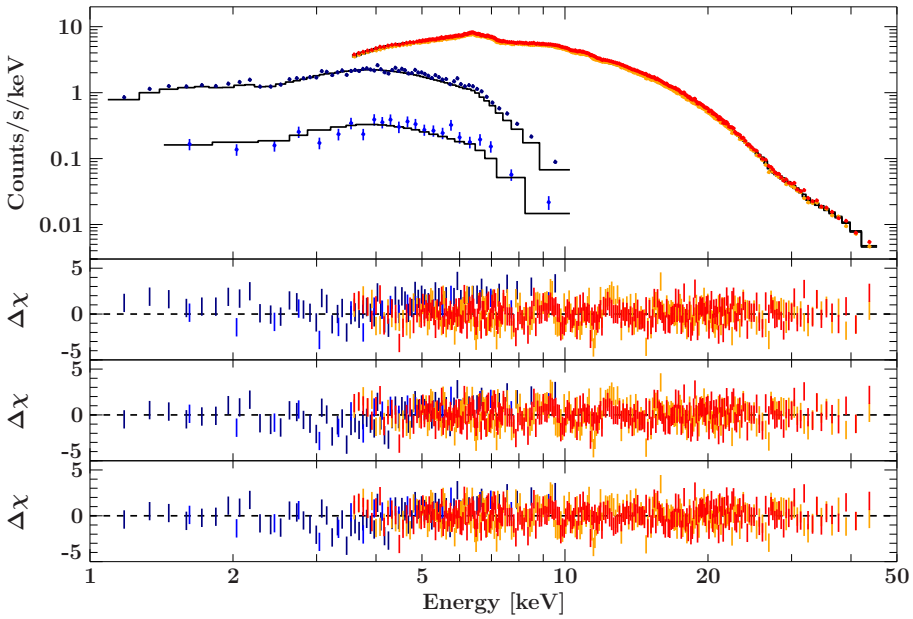

Figure 21: Spectum of Cen X–3 as seen by *NuSTAR* and *Swift*. The upper panel shows the the spectrum fitted with `BWsim`. In red and orange the data from the two focal plane modules of *NuSTAR* is shown and in dark and light blue the *Swift* data in window timing and photon counting mode. The first residual panel shows the the residuals for `BWsim`, the second one for *FDcut* and the third for the `highcut` model.

can lead to unphysically broad and deep lines. In order to probe such a dependency, the spectrum was described described with the cut-off model `fdcut` as well as with `highcut` (Müller et al., 2013).

With a $\chi^2_{\rm red}$ of 1.32 and 1.28 for 450 and 453 d.o.f., respectively, both describe the spectrum spectrum reasonably well. Since `highcut` has a discontinuity at the cut-off energy it needs an additional broad absorption component tied to that energy. Incidentally, this gets rid of some residuals caused by calibration issues between 10 and 14 keV (see Wolff et al., 2016, and references therein), which leads to a slightly lower $\chi^2_{\rm red}$ value. The final model includes a calibration constant, $C_{\rm det}$, as well as a partial absorber, three narrow iron lines (i.e., a width smaller than the detector resolution), and one broad Gaussian component, the so-called "10 keV feature", and the cyclotron resonance feature around 30 keV, which we model by a multiplicative Gaussian absorption component (`gabs`). In summary the full model is

$$C_{det} \times tbnew_{feo} \times tbnew_{pcf} \times (powerlaw \times fdcut + gaussian_{3+1\,\rm ironlines} + gaussian) \times gabs. \quad (18)$$

The parameters for the corresponding best-fits are given in Table **??**. The residuals of the fit are shown in Fig. 21 (middle residual panel). As noted previously by, e.g., Burderi et al. (2000), Cen X–3 features very prominent fluorescent iron lines between 6 and 7 keV. Most prominently the neutral Kα line at 6.4 keV but also higher ionization states of He- and H-like iron at 6.7 keV and 6.97 keV.

When excluding the additional partial coverer we found, that the spectrum can no longer be

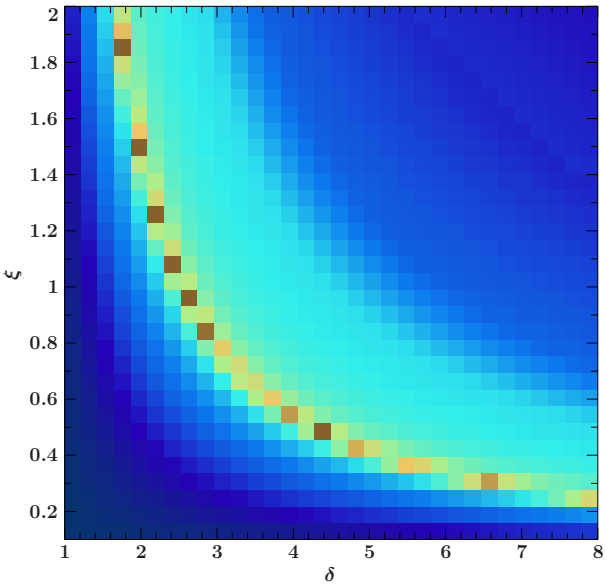

Figure 22: Confidence contour for the `BWsim` parameters ξ and δ. The severe degeneracy between the parameters is clearly visible.

modelled at energies below 2 keV, leading to a $\chi^2_{\rm red}$ of 1.65. It should be noted, that this deviation and, thus, the existence of the partial coverer is only significant when *Swift*-XRT data is included in the fit. These results fit well to previous fits to Cen X–3 spectra (Marcu et al., 2015; Naik et al., 2011).

As a next step, the physical model `BWsim` was applied to the spectra. The full model is defined as

$$C_{det} \times tbnew_{feo} \times tbnew_{pcf} \times (zashift((BWsim + gaussian) \times gabs) + gaussian_{3+1\,\rm ironlines}). \quad (19)$$

Since `BWsim` calculates the emitted radiation in the reference frame of the neutron star, it is necessary to modify the continuum with *zashift*, which accounts for the gravitational redshift. In contrast to other sources (Wolff et al., 2016), for Cen X–3, `BWsim` alone for could not account for the "10 keV feature" of Cen X–3 and a broad Gaussian had therefore to be included as part of the continuum again.

Initially the iterative approach was used to fit the described model. The resulting best fit had a reduced χ^2 of 1.32 with 601 d.o.f. and the remaining residuals are shown in Fig. 21 and the best-fit parameters are listed in Table 2.

With the new fitting approach, i.e., including a χ^2-penalty (see Eq. 17) almost identical results were obtained, with the one exception, that the accretion rate slightly different compared to the iterative approach (see best-fit parameters in Table 2). The corresponding parameters are listed in Table 2. However, some of the fit-parameters of the `BWsim` model are degenerate, e.g., δ and ξ as shown in Fig. 22. Thus, the 90% uncertainties given in Table 2 should be taken with care since they are calculated assuming uncorrelated parameters in XSPEC and ISIS.

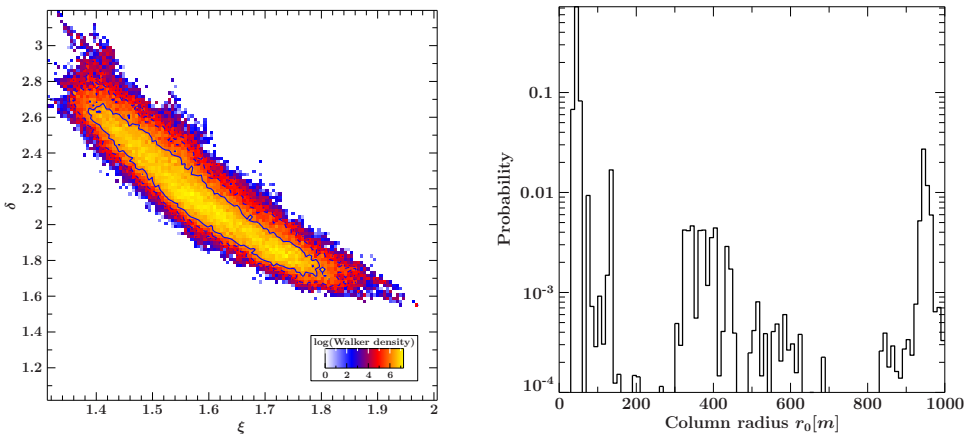

Figure 23: Preliminary results of applying the the MCMC method the *BWsim*. While the used chains already show interest features in the χ^2 landscape Left: Two-dimensional histogram of the walker distribution after 5000 iterations. The sold and dashed blue line indicated the 1σ and 2σ contours. Right: One-dimensional histogram showing the walker distribution for the column radius, scaled logarithmically.

7.1.4 The MCMC hammer

To further constrain parameter degeneracies and a handle in the χ^2 landscape, with and without the χ^2 tweak adjusting energy conservation, it was tried to use Markov chain Monte Carlo to sample the parameter space. To this end the *ISIS* implementation of the MCMC Hammer code (Foreman-Mackey et al., 2013) was used. This Bayesian method has the big advantage of sampling the entire parameter space at once it is therefore possible to see the degeneracies between each set of parameters. In this approach a larger number of "walkers" (about 100-200) are distributed over the parameter space. Over many iteration these walker randomly update their position in parameter space based on the χ^2 landscape. After enough iterations the walker distribution will be stable and, as one can show, proportional to the χ^2 landscape. However, the big disadvantage compared to traditional χ^2 minimization is the significantly increased computation time. The time needed for the walker distribution to converge is further increased if the χ^2 landscape is complex with multiple local minima in which the walker can get stuck in. This is what happened several time in the course of this work, delaying the the result beyond the scale of the thesis. Nonetheless, even the partially converged parameter chain can give valuable insight in the in the χ^2 landscape of *BWsim*. Fig. 23 shown clearly the the strong parameter correlation that has already been observed by classically scanning the parameter space (see Fig. 22). This already shows the potential of the MCMC algorithm. It is also instructive to consider the distribution in the Column Radius of *BWsim*, shown on the right in Fig. 23. Two prominent walker populations at the high and the low end of the parameter a weak one in the middle can clearly be seen. This distribution indicates, that good fits can be found at both ends of the parameter range. This will become important when comparing the best-fit parameter to previous results.

7.1.5 Discussion

In the following the best-fit parameters obtained by the new fitting approach are discussed. An accretion rate of $1.66 \times 10^{17}\,\mathrm{g\,s^{-1}}$ was obtained. Together with the unabsobed model luminosity of $2.05 \cdot 10^{37}\,\mathrm{erg\,s^{-1}}$ this places Cen X–3 firmly in the regime of a radiation-dominated shock (Kühnel et al., 2017a), which is necessary to justify the application of`BWsim`.

The best-fit has a column radius of just 63 m, which is just a fraction of the 730 m estimated by BW07. However, BW07 used data when Cen X–3 had a luminosity of $\sim 2.54 \times 10^{37}\,\mathrm{ergs\,s^{-1}}$, still assuming a distance of 5.7 kpc, compared to $1.71 \times 10^{37}\,\mathrm{ergs\,s^{-1}}$ for the more recent *NuSTAR* observation. This lower accretion rate allows a wider Alfvén radius and, according to Eq. 110 in BW07 a smaller accretion column. However, the column radius only depends on $L_X^{1/7}$, which, for these luminosities can only accounts for a variation of ∼10%. More rigorous application of BW07 to Cen X–3 have been presented by Gottlieb et al. (2016) and will be published by Marcu-Cheatham et al. (in prep.). These fits, too, present a column radius around 65 in line for the results presented here. As the preliminary MCMC analysis has already shown, it is therefore likely that the large deviation between the column radius presented here and in BW07 can be attributed to the "by-eye" fitting in BW07, which can be quite unreliable to such complex models with multiple solutions, such as *BWsim*.

Following Davidson & Ostriker (1973), one can give an theoretical estimate for the column radius from the accretion rate and the magnetic field strength assuming a dipole geometry. Equating the pole radius r_{pole} used by Davidson & Ostriker (1973) with the column radius r_0 , it follows that

$$r_0 \approx R_0^{3/2} R_{\mathrm{m}}^{-1/2}, \tag{20}$$

where R_0 is the radius of the neutron star and R_m is the Alfvén radius which is given by

$$R_{\mathrm{m}} = (2.4 \times 10^8 \mathrm{cm}) \left(\frac{B_0}{10^{12}\mathrm{G}}\right)^{4/7} \left(\frac{R_0}{10\,\mathrm{km}}\right)^{12/7} \times \left(\frac{\dot{M}}{10^{17}\,\mathrm{g\,s^{-1}}}\right)^{-2/7} \left(\frac{m_{\mathrm{NS}}}{M_\odot}\right)^{-1/7}, \tag{21}$$

where B_0 is the magnetic field strength obtained from the fit, $\dot{M}$ is the accretion rate and m_{NS} is the mass of the neutron star. This equation gives an Alfvén radius of 3377 km and a column radius of $r_0 = 511$ m; far wider than the best-fit would suggest. Compared to BW07 ξ and δ are of a similar order , but lower value of δ was obtained indicating a higher importance of thermal compared to bulk Comptonization. However, as Fig. 22 shows, there is very significant degeneracy between ξ and δ. This degeneracy limits the scientific significance of these values.

The obtained Compton Temperature of 4.52 keV far exceeds the corresponding Eddington Temperature, which is reasonable considering fan type emission pattern.

In order to further assess how physical the derived parameters are, we can calculate the integration height z_{max} and the height of the sonic point z_{sp} according to E1. 80 and Eq. 31 of BW07. One finds $z_{\mathrm{max}} = 5.2$ km and $z_{\mathrm{sp}} = 2.6$ km. Therefore the sonic shock lies within the integration region, as it is supposed to. Further, the "blooming fraction" at the sonic point can be obtained, which is given by $((R_{\mathrm{NS}} + z_{\mathrm{sp}})R_{\mathrm{NS}})^3$ to be 2.0. This value, which clearly exceeds unity, indicates

Table 1: Best-fit parameters for different empirical models

Parameter	Highcut	FDcut
N_H (cm^{-2})	1.71 ± 0.28	1.62 ± 0.28
$N_{\mathrm{H/pcf}}$ (cm^{-2})	$10.8^{+1.1}_{-1.0}$	10.3 ± 1.0
pcf	$0.798^{+0.030}_{-0.033}$	0.78 ± 0.04
$\mathrm{Norm_{PL}}$	$0.205^{+0.033}_{-0.022}$	$0.178^{+0.019}_{-0.015}$
Γ	$1.17^{+0.10}_{-0.07}$	1.05 ± 0.07
E_{cutoff} (keV)	$12.67^{+0.17}_{-0.15}$	22^{+6}_{-5}
E_{Fold} (keV)	$9.6^{+0.7}_{-0.4}$	$6.1^{+0.9}_{-1.3}$
σ_{gabs} (keV)	$1.63^{+0.35}_{-0.27}$	—
$\mathrm{A_{gabs}}$	$0.29^{+0.15}_{-0.10}$	—
$\mathrm{A_{6.4\,keV}}$	$\left(1.22^{+0.17}_{-0.18}\right) \times 10^{-3}$	$\left(1.24^{+0.18}_{-0.19}\right) \times 10^{-3}$
$\mathrm{A_{6.7\,keV}}$	$(2.4 \pm 1.4) \times 10^{-4}$	$\left(2.9^{+1.6}_{-1.5}\right) \times 10^{-4}$
$\mathrm{A_{6.97\,keV}}$	$(5.3 \pm 1.5) \times 10^{-4}$	$\left(5.9^{+1.6}_{-1.5}\right) \times 10^{-4}$
$\mathrm{A_{broad}}$	$(4.3 \pm 0.6) \times 10^{-3}$	$\left(3.9^{+0.6}_{-0.7}\right) \times 10^{-3}$
$\mathrm{E_{broad}}$ (keV)	6.23 ± 0.08	$6.21^{+0.08}_{-0.09}$
σ_{broad} (keV)	0.55 ± 0.06	0.51 ± 0.06
$\mathrm{A_{10\,keV}}$	$0.018^{+0.013}_{-0.007}$	$\left(9.7^{+3.7}_{-2.7}\right) \times 10^{-3}$
$\mathrm{E_{10\,keV}}$ (keV)	$13.5^{+1.0}_{-1.2}$	12.6 ± 0.4
$\sigma_{\mathrm{10\,keV}}$ (keV)	4.1 ± 0.6	$2.9^{+0.5}_{-0.4}$
$\mathrm{E_{CRSF}}$ (keV)	$29.6^{+0.5}_{-0.4}$	$28.90^{+0.36}_{-0.29}$
σ_{CRSF} (keV)	3.8 ± 0.5	$6.3^{+0.9}_{-1.1}$
$\mathrm{A_{CRSF}}$	2.7 ± 0.7	13^{+10}_{-6}
$\mathrm{C_{FPMB}}$	1.0256 ± 0.0022	1.0255 ± 0.0022
$\mathrm{C_{PC}}$	0.76 ± 0.06	0.76 ± 0.06
$\mathrm{C_{WT}}$	1.076 ± 0.017	1.075 ± 0.017

that the assumption of cylindrical symmetry is not quite accurate. Similarly we can calculate the magnetic field strength at the sonic point to be $1.6B_{12}$, which also indicates that the assumption of a constant magnetic field is not fulfilled. However, this should not distort out results too much as must of the photons are emitted in the regions of highest densities, i.e., below the sonic point at the very bottom of the accretion column (Wolff et al., 2016).

Table 2: Best-fit parameters with for the `BWsim` model fits

Parameter	χ^2 method	iterative method
$N_{\rm H}$ (cm^2)	$1.37^{+0.28}_{-0.26}$	$1.36^{+0.29}_{-0.25}$
$N_{\rm H/pcf}$ (cm^2)	$10.3^{+1.0}_{-0.7}$	$10.3^{+1.1}_{-0.6}$
pcf	0.77 ± 0.04	0.78 ± 0.04
$\dot{M}$ $1.67^{+0.05}_{-0.06}$	1.73	
$kT_{\rm c}$ (keV)	$4.53^{+0.11}_{-0.13}$	$4.51^{+0.10}_{-0.08}$
r_0 (m)	$63.4^{+2.7}_{-3.9}$	67^{+6}_{-9}
B (10^{12}G) [5]	3.29	3.31
ξ	$1.61^{+0.14}_{-0.12}$	$1.58^{+0.13}_{-0.11}$
δ	$2.04^{+0.32}_{-0.23}$	$2.10^{+0.23}_{-0.16}$
$A_{10\,\rm keV}$	$\left(8.1^{+4.2}_{-2.2}\right) \times 10^{-3}$	$\left(7.9^{+4.3}_{-2.2}\right) \times 10^{-3}$
$E_{10\,\rm keV}$	$16.6^{+0.4}_{-0.5}$	16.6 ± 0.4
$\sigma_{10\,\rm keV}$	$3.3^{+0.6}_{-0.5}$	$3.3^{+0.6}_{-0.5}$
$E_{\rm CRSF}$ (keV)	$38.15^{+0.43}_{-0.29}$	$38.14^{+0.43}_{-0.27}$
$\sigma_{\rm CRSF}$ (keV)	$8.7^{+0.5}_{-0.4}$	8.8 ± 0.4
$\rm A_{CRSF}$	$22.3^{+2.1}_{-1.7}$	$22.6^{+2.1}_{-1.8}$
$\rm A_{6.7\,keV}$	$\left(1.25^{+0.19}_{-0.18}\right) \times 10^{-3}$	$\left(1.26^{+0.17}_{-0.19}\right) \times 10^{-3}$
$\rm A_{6.9\,keV}$	$\left(2.8^{+1.5}_{-1.4}\right) \times 10^{-4}$	$\left(2.9^{+1.5}_{-1.4}\right) \times 10^{-4}$
$\rm A_{broad}$	$\left(6.0^{+1.6}_{-1.4}\right) \times 10^{-4}$	$(6.1 \pm 1.5) \times 10^{-4}$
$\sigma_{\rm broad}$ (keV)	$(3.9 \pm 0.6) \times 10^{-3}$	$\left(3.9^{+0.5}_{-0.7}\right) \times 10^{-3}$
$C_{\rm FPMB}$	$6.21^{+0.08}_{-0.09}$	$6.20^{+0.08}_{-0.09}$
$C_{\rm PC}$	0.52 ± 0.06	$0.52^{+0.05}_{-0.06}$
$C_{\rm WT}$	0.76 ± 0.06	0.76 ± 0.06

7.2 NICER observation of Cen X–3

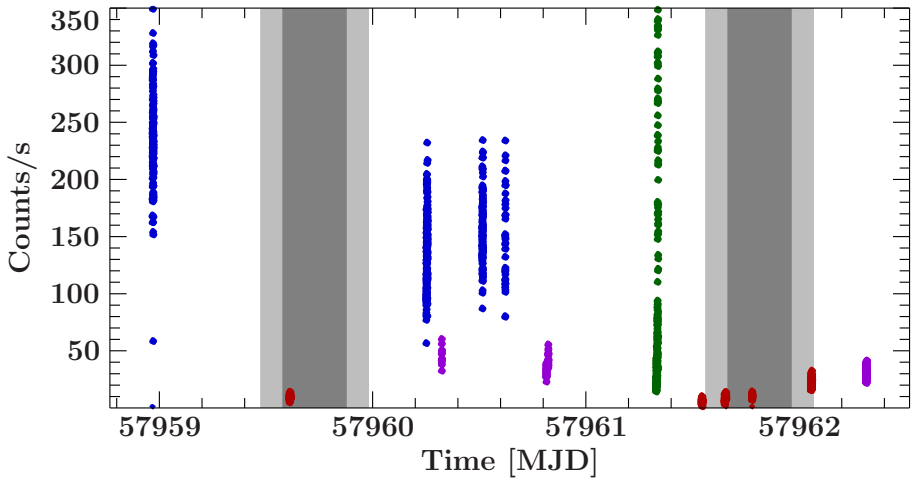

Figure 24: *NICER* lightcurve of Cen X–3 over for the July 2017 observation binned to the pulse period of ∼2.8 s. The gray bars indicate the expected position of the eclipse extrapolated from orbit measurements by Falanga et al. (2015). The "unobscured" observations as shown in blue, the "partially obscured" in violet and the "eclipsed" ones in red. Green marks the particle induced background flare near the "polar horn"

As discussed in chapter 7, Cen X–3 features an eclipse, which covers 10%-20% of its orbit. To fully understand this source it is therefore essential to take data over the complete orbit. Such an observation has been performed previously with *Suzaku* (Naik et al., 2011), *ASCA* (Ebisawa et al., 1996) and most recently with *NICER*.

This section will describe the extraction and analysis of the new *NICER* data and will compare the result to previous observations.

7.2.1 Observation & Data Reduction

The *NICER* observation took place on from 2017 July 24 to July 27 as part of the *NICER*'s calibration phase, which was interest in observing previously studied emission lines. The observation consists of twelve distinct pointings and covers two eclipses. These pointings a grouped in five ObsIDs (1034070101–1034070105) and have a total exposure time of 10.5 ks.

During ObsID 1034070104 the ISS passed though the southern 'polar horn' area, a region where the outer Van Allen radiation belts reaches the low-earth orbit [6]. These belts harbour an increased density of energetic electrons (see Pierrard et al., 2014, for more detail on the particle background in LEO). This led to an increased background at high energies (>8 keV). Luckily, after the update to HEAsoft 6.26 this flares are detected and removed be the adjusted filter criteria of the *NICER* extraction pipeline.

[6] `https://heasarc.gsfc.nasa.gov/docs/nicer/science_nuggets/20180809.ht`

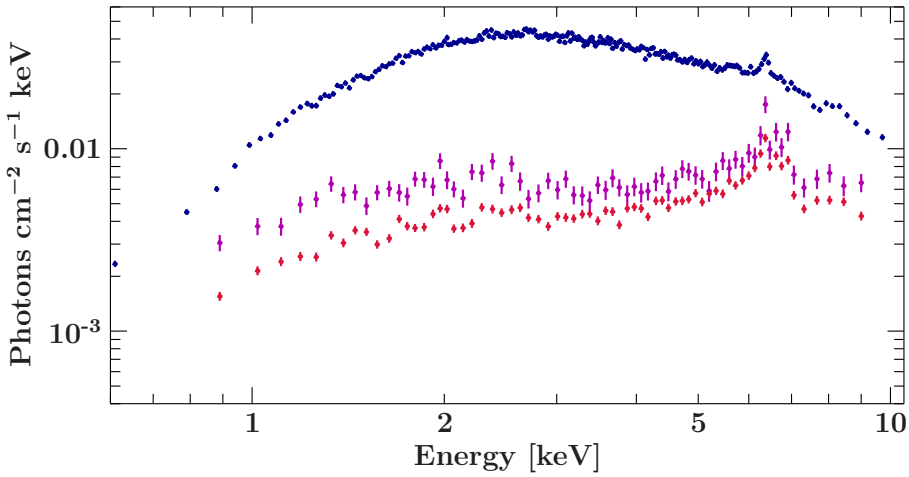

Figure 25: Spectra for the three different source states. Blue indicated the unobscured state, violet the partially obscured one and red the eclipse

The cleaned light curve can be seen in Fig. 24. Due to the comparably short exposure time, however, the orbit is not as densely covered as by previous, e.g., *Suzaku* observations. To improve the signal-to-noise ratio, the data was therefore initially binned into three source states, which were labels "unobscured","partially obscured" and "eclipse" (see Fig 24).

As the "partially obscured" and "eclipse" spectrum were very similar, as becomes clear from Fig. 25, and the only had a very limited SNR they were combined and only two states were distinguished in the final analysis.

7.2.2 Results

The final fits to the two resulting spectra are shown in Fig. 27 & Fig. 27. While the the neutron star during "eclipse" state is obviously shrouded by the optical companion and material close to it, during "partially obscured" state high density structures in the wind. A similar decrease in luminosity prior to the eclipse is well known in Cen X–3 (Nagase et al., 1992; Naik et al., 2011) and is likely caused by the accretion wake trailing behind the neutron star in its orbit.

The fit to the unobscured spectra shows the familiar features, that have already been seen in the *Swift* and *NuSTAR* spectrum. Namely are power-law continuum with a photon index around one. With 1.3 it is slightly higher than for than previously. Due to the smaller energy range however the continuum is generally less constrained by *NICER* alone and smaller such deviations are therefore not unexpected. Additionally the steeper spectral index might also hint so slight internal changes in the accretion geometry between the two observations (Kühnel et al., 2017b; Reig & Milonaki, 2016; Malacaria et al., 2015). Due to the limited wavelength coverage it is of courses also not possible to get any information about high energy features such as the cut-off, the 10 keV feature of even the CRSF.

To directly compare the new *NICER* observation with previous observations, *Suzaku*/XIS data with the ObsID 403046010 were extracted. For the extraction Heasoft 6.26 with Suzaku CalDB

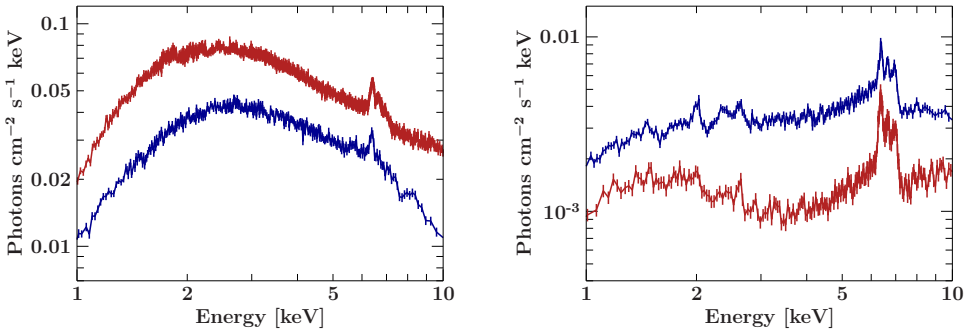

Figure 26: Comparison between the spectrum seen by *NICER* (blue) and *Suzaku* (red)

vers. 20181010 was used. The source spectra were extracted from an annulus outer radius of 70″ and inner radius of big enough to exclude region with a pile-up of more than 4%. The background spectra were extracted from circular regions at the edges of the detectors with a diameter of 100″. The comparison between the *NICER* and the *Suzaku* data is shown in Fig. 26. It shows, that the overall shape of the spectra is similar, nevertheless, the *NICER* observations show several deviation from the previous observation. The most apparent difference is the smaller extend to which the luminosity changes between the two source states. While for flux during the *Suzaku* observation changed by a factor of ∼24 while the two spectral states discussed here only differ by a factor of ∼4.4 in luminosity. To some extent, this might be due to a change in the source activity and amount of material surrounding the neutron star. However, the increased luminosity in the low state can be traced back to the more generous grouping for the *NICER* observation, which also included observation outside of the eclipse. Additionally, due to the scarce sampling eclipse as well as the complete unobscured state might not be observed exactly, further smearing out the luminosity contrast.

Towards the obscured low luminosity state, the spectrum changes drastically. As most of the radiation gets absorbed and only reprocess radiation reaches the observer, the continuum also get more complex. Additionally, the grouping of different pointing, that was necessary to increase the SNR, led to combination of observation at different time and orbital phases. Consequently the observed radiation most likely comes from regions of varying density and ionisation. As such, an absorbed power-law as a continuum model becomes overly simplistic, leaving residuals especially in the range of 3–6 keV, where no strong emission lines have previous been seen (Naik et al., 2011; Ebisawa et al., 1996; Iaria et al., 2005a). Due to the limited available energy range and SNR, however, it was not possible exactly constrain the continuum. To better model the continuum around the iron line complex a broad Gaussian was introduced, which led to a significantly improved fit. This, more empirical that physically motivated component, at least partially accounts for several effects such a Compton shoulder and the clearly visible Iron K-edge that lead to complex structures around the Iron-complexes. There are more phsical models to describe such hot plasma, namely *mekal*(Mewe et al., 1985) and *apec*[7] for collisional ionization and *XSTAR*[8] for photo-

[7]For more information see: `http://atomdb.org/`
[8]For more information see: `https://heasarc.nasa.gov/docs/software/xstar/xstar.html`

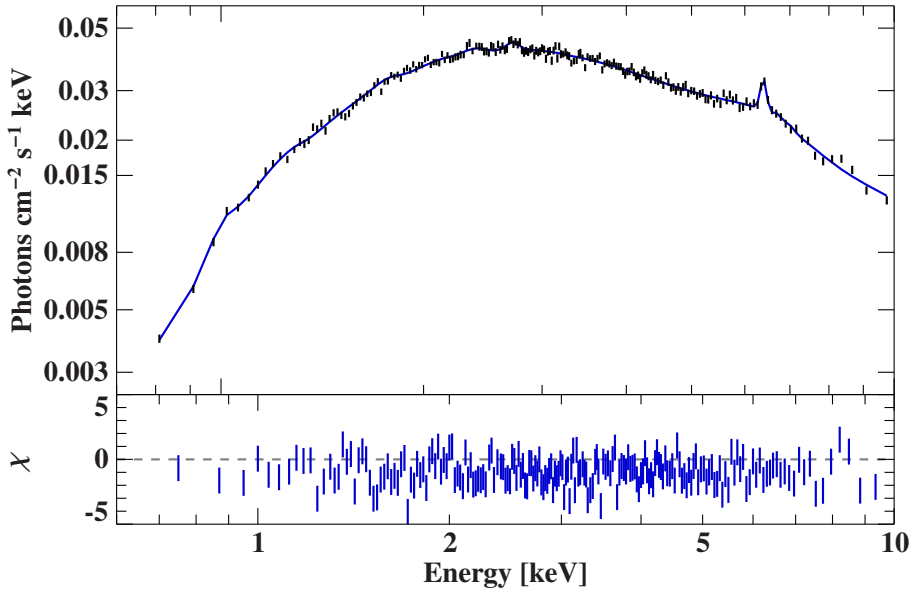

Figure 27: *NICER* spectrum of Cen X–3 during the unobscured high luminosity state, include the best-fit model.

ionization. *mekal* and *apec* could not deliver acceptable fits, has the intense radiation inside Cen X–3 leads to a highly photo-ionized plasma. Using *XSTAR*, however to try to, model the complex ionization was beyond the scope of this these and would most likely require data with a higher spectral resolution to produce reliable result.

Table 3: Observer emission lines, their observed lines (uncertainties can be found in Tab. 4), and the respective literature values.

	observed Energy [keV]	literature value[9] [keV]
Ne X Lα	1.043	1.0218
Mg XII Lα	1.40	1.4723
Si XIV Lα	2.008	2.0055
Si XIV Lβ	2.400	2.3765
S XVI Lα	2.615	2.621
Fe I Kα	6.396	6.40
Fe XXV Heα	6.693	unloved triplet
Fe XXVI Lyα	6.963	6.9661

The most descriptive feature in this during the low luminosity state are by far the numerous detected emission lines. There observed energies and the respective literature values can be found in Tab. 3. Several line originating from highly ionized hydrogen-like ions of Ne, Mg, Si and S are detected. All these emission lines have already been detected in Cen X–3 by Naik et al. (2011). The fact there are no helium-like lines seen already indicated, that the gas producing these lines is highly ionized. Ebisawa et al. (1996) used XSTAR simulations to estimate the ionisation parameter

[9]Literature values adapted from Drake (1988), Krause & Oliver (1979), Garcia & Mack (1965) and Johnson & Soff (1985)

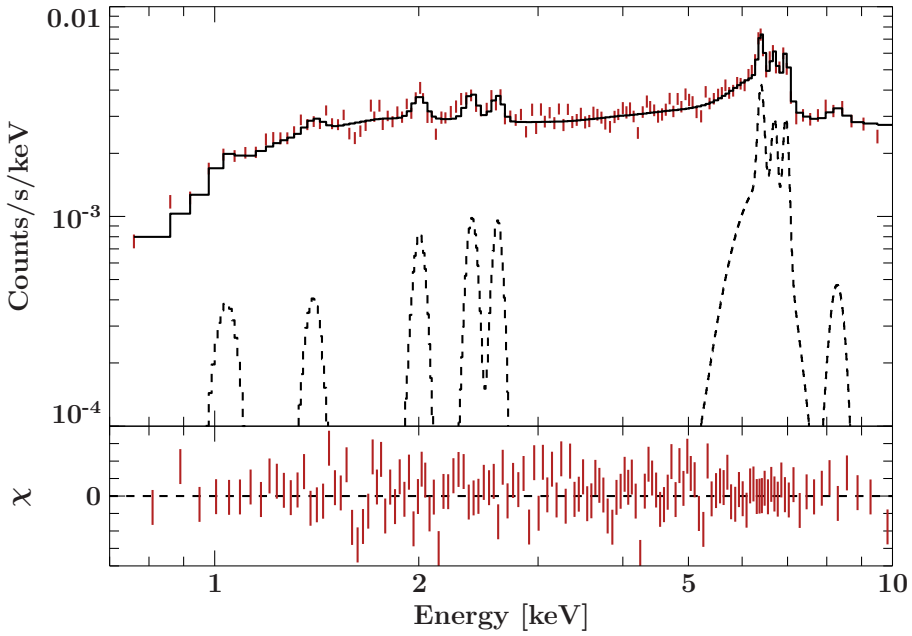

Figure 28: *NICER* spectrum of Cen X–3 during the eclipse. In red is shown the best-fit and its residuals in the lower panel. The line emission is shown as dotted lines. (Update with better fit.)

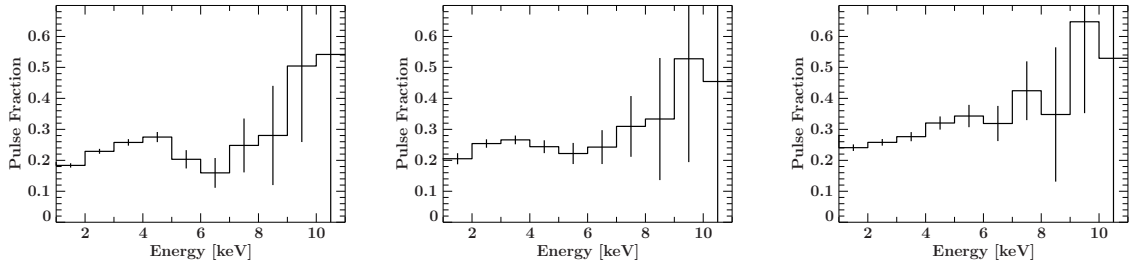

Figure 29: Pulse fraction during the bright states see in Fig.24. Notice the reduced pulsation strength around the iron line.

ξ to be in the order of $10^{3.4}$.

The detection of neutral iron however, indicated at-least two separate emission regions. This is supported by the changing flux rations in the iron emission lines. Outside of the eclipse only the neutral iron line is detected, while the ones from higher ionisation states disappear in the continuum. Only the Ne emission line slightly detected, however a more detailed analysis would be need to constrain its precise significance. This shows that the extend of the less ionized emission region must be see than the extent of the donor star $\sim 8 \times 10^{11}$ cm. Observing how fast the line emission drops of at the onset of an eclipse Nagase et al. (1992) could even constrain the extent to be less than $\sim 3 \times 10^{10}$ cm.

To further constrain the origin of the iron line one can have a look at the pulse traction in different energy band. Fluorescence lines that originate from a larger radius are not to show strong pulsation as the arrival time is smeared out by travel tie of the photons. The result of such an

Table 4: Best-fit parameters for the two different source states

Parameter	Obscured State
N_{H1}	0.79 ± 0.07
N_{H2}	31^{+7}_{-6}
pcf	$0.53^{+0.07}_{-0.09}$
Norm(PL)	$0.0114^{+0.0032}_{-0.0025}$
Γ	0.57 ± 0.12
norm	$\left(2.8^{+1.8}_{-1.5}\right) \times 10^{-4}$
E [keV]	$1.043^{+0.028}_{-0.023}$
norm	$\left(1.6^{+0.9}_{-0.8}\right) \times 10^{-4}$
E [keV]	$1.40^{+0.08}_{-0.04}$
norm	$\left(2.5^{+0.9}_{-0.8}\right) \times 10^{-4}$
E [keV]	$2.008^{+0.018}_{-0.008}$
norm	$\left(2.8^{+1.2}_{-1.0}\right) \times 10^{-4}$
E [keV]	$2.400^{+0.016}_{-0.045}$
norm	$\left(2.7^{+1.1}_{-1.0}\right) \times 10^{-4}$
E [keV]	$2.615^{+0.021}_{-0.024}$
norm	$(5.3 \pm 1.4) \times 10^{-4}$
E [keV]	$6.396^{+0.020}_{-0.011}$
norm	$(3.3 \pm 1.4) \times 10^{-4}$
E [keV]	$6.694^{+0.022}_{-0.034}$
norm	$(4.1 \pm 1.4) \times 10^{-4}$
E [keV]	$6.963^{+0.017}_{-0.034}$
norm	$\left(2.1^{+0.7}_{-0.6}\right) \times 10^{-3}$
E [keV]	$6.37^{+0.11}_{-0.13}$
σ	$0.51^{+0.14}_{-0.11}$
norm	$\left(3.0^{+2.5}_{-2.6}\right) \times 10^{-4}$
E [keV]	$8.3^{+0.4}_{-3.6}$
σ	$0.20^{+0.00}_{-0.20}$
$red.\chi^2/d.o.f$	1.53 / 108

Parameter	Unobscured state
N_{H1}	$1.29^{+0.05}_{-0.04}$
N_{H2}	$4.23^{+0.24}_{-0.22}$
pcf	$0.713^{+0.019}_{-0.017}$
norm	$0.267^{+0.029}_{-0.019}$
Γ	$1.33^{+0.08}_{-0.05}$
norm	$\left(9.4^{+37253.9}_{-2.8}\right) \times 10^{-3}$
E [keV]	$6.40^{+0.15}_{-0.14}$
σ	$0.97^{+0.41}_{-0.25}$
norm	$(6.9 \pm 2.8) \times 10^{-4}$
E [keV]	$2.713^{+0.029}_{-0.031}$
norm	$(3.3 \pm 1.7) \times 10^{-3}$
E [keV]	$1.009^{+0.036}_{-0.015}$
$red.\chi^2/d.o.f$	1.05/ 535

analysis for the three brightest pointing is shown in Fig. 29. Especially during the fist observation in the unobscured state a clear drop in the 6–7 keV range is visible. This is also, even if less pronounced, seen in the other observation. Together with the different degrees of ionisation and flux evolution over the orbits this clearly demonstrates, that the less ionized material mus reside close to the neutron star while the highly ionized plasma engulfs the system at a much higher radius.

8 Conclusion & Outlook

These thesis first presents the analysis of combined *NuSTAR* and *Swift* spectra of Cen X–3. To simplify application of physical model to the spectrum of accreting pulsar, a new approach of fitting the model *BWsim* by BW07 was introduced. By increasing the value of χ^2 for unphysical parameter ranges, it was possible to apply the physical model derived by BW07 without having to assure energy conservation in any other, external way. This will, in many cases, simplify its usage considerably. With this new approach previous fits to the the spectrum of Her X-1 were reproduced and the spectrum of Cen X–3 would be described. Features which have been seen in previous works were found, i.e., prominent iron lines (Ebisawa et al., 1996), a CRSF at ≈ 3 keV and a partially absorbed power-law (Suchy et al., 2008) and the parameters of *BWsim* describing the accretion column agreed with previous applications of the model to other datasets of Cen X–3. For both Cen X–3 and Her X-1 *BWsim* could, therefore, describe the spin-averaged spectrum well and we reached fits with similar quality as conventional phenomenological models. This new approach is one step towards the more frequent application of physical models to the complex nature of X-ray pulsar, which will be necessary to gain a deeper understanding from the already available data. However, some of the issue related to *BWsim*, such as the strong degeneracy between many of its parameters (e.g., ξ and δ) and the need for a strong "10 keV bump", still subsist. In order to qualify some of issues it is insightful to map the whole parameter space with tools like the MCMC algorithms. Initial steps in this direction have been made and will hopefully be part of a future publication. The rest of this thesis was then concerned with the analysis of data from *NICER*. The data from the most recent outburst of 4U 1901+03 is presented not indication no strong change in the accretion geometry. However, a now detailed analysis of this rich dataset will be part of a forthcoming publication by Coley and others. Part of such an analysis could be detailed description of the pulse profile evolution over the course of the outburst. Especially at the very maximum of it luminosity, changes in the accretion behaviours might be detectable. This could be combined with a spectral analysis going beyond the simplified look at the hardness ratio. The additional available *NuSTAR* data will provide a handle continuum emission and give details about the possible detection of a CSRF. To connect the two central topics of this thesis, Cen X–3 and *NICER*, an observation of Cen X–3 that *NICER* performed as part of its calibration phase was analysed. While the total exposure time was limited and similar observations have been previously performed with *Suzaku* and *ASCA*, their results could be reproduced, demonstrating *NICER*'s capabilities and highlighting its outstanding effective area. In the future the goal will be combining models of the accretion column such as BW07 with relativistic light-bending codes to fully describe the time and energy dependent X-ray emission from accretion X-ray pulsars. This will be a huge step forward and *NICER*'s high time resolution will make it the ideal instrument for testing such self-consist models in the soft X-rays and further assist the transition away from merely applying empirical models towards really understanding the underlying physics.

References

Arzoumanian Z., Gendreau K.C., Baker C.L., et al., 2014, Space Telescopes and Instrumentation 2014: Ultraviolet to Gamma Ray 9144, 914420

Ash T.D.C., Reynolds A.P., Roche P., et al., 1999, MNRAS307, 357

Bailer-Jones C.a.L., Rybizki J., Fouesneau M., et al., 2018, The Astronomical Journal 156, 58

Balsamo E., Gendreau K., Okajima T., et al., 2016, Journal of Astronomical Telescopes, Instruments, and Systems 2, 015001

Bartels J., Heck N.H., Johnston H.F., 1939, Terrestrial Magnetism and Atmospheric Electricity (Journal of Geophysical Research) 44, 411

Barthelmy S.D., Barbier L.M., Cummings J.R., et al., 2005, Space Science Reviews 120, 143

Becker P.A., Klochkov D., Schönherr G., et al., 2012, Astronomy and Astrophysics 544, A123

Becker P.A., Wolff M.T., 2007, ApJ654, 435

Becker P.A., Wolff M.T., 2007, The Astrophysical Journal 654, 435

Bissinger M., 2016, doctoralthesis, Friedrich-Alexander-Universität Erlangen-Nürnberg (FAU)

Boldin P.A., Tsygankov S.S., Lutovinov A.A., 2013, Astronomy Letters 39, 375

Bondi H., 1952, MNRAS112, 195

Bondi H., Hoyle F., 1944, MNRAS104, 273

Brumback M.C., Hickox R.C., Fürst F.S., et al., 2018, ApJ852, 132

Burderi L., Di Salvo T., Robba N.R., et al., 2000, ApJ530, 429

Burderi L., Salvo T.D., Robba N.R., et al., 2000, The Astrophysical Journal 530, 429

Burrows D.N., Hill J.E., Nousek J.A., et al., 2005, Space Sci. Rev.120, 165

Conti P.S., McCray R., 1980, Science 208, 9

D'Angelo C.R., Spruit H.C., 2012, MNRAS420, 416

Davidson K., Ostriker J.P., 1973, ApJ179, 585

Drake G.W., 1988, Canadian Journal of Physics 66, 586

Ebisawa K., Day C.S.R., Kallman T.R., et al., 1996, PASJ48, 425

Falanga M., Bozzo E., Lutovinov A., et al., 2015, Astronomy and Astrophysics 577, A130

Falkner S., Schwarm F.W., Wolff M.T., et al., 2016, In: AAS/High Energy Astrophysics Division #15. AAS/High Energy Astrophysics Division, p. 201.08

Foreman-Mackey D., Hogg D.W., Lang D., Goodman J., 2013, PASP125, 306

Forman W., Jones C., Tananbaum H., 1976, The Astrophysical Journal 208, 849

Frank J., King A., Raine D.J., 2002, Accretion Power in Astrophysics: Third Edition

Garcia J.D., Mack J.E., 1965, Journal of the Optical Society of America (1917-1983) 55, 654

Gehrels N., Chincarini G., Giommi P., et al., 2004, ApJ611, 1005

Gehrels N., Chincarini G., Giommi P., et al., 2004, The Astrophysical Journal 611, 1005

Gendreau K.C., Arzoumanian Z., Okajima T., 2012, Amsterdam, Netherlands, p. 844313

Ghosh P., Lamb F.K., 1979, ApJ234, 296

Giacconi R., Gursky H., Kellogg E., et al., 1971, ApJ167, L67

Gottlieb A., Pottschmidt K., Marcu D., et al., 2016, In: AAS/High Energy Astrophysics Division #15. AAS/High Energy Astrophysics Division, p. 120.09

Gvaramadze V.V., Gräfener G., Langer N., et al., 2019, Nature 569, 684

Harding A.K., Meszaros P., Kirk J.G., Galloway D.J., 1984, ApJ278, 369

Harrison F.A., Craig W.W., Christensen F.E., et al., 2013, The Astrophysical Journal 770, 103

Harrison F.A., Craig W.W., Christensen F.E., et al., 2013, ApJ770, 103

Hirsch M., Hell N., Grinberg V., et al., 2019, A&A626, A64

Houck J.C., Denicola L.A., 2000, In: Manset N., Veillet C., Crabtree D. (eds.) Astronomical Data Analysis Software and Systems IX, Vol. 216. Astronomical Society of the Pacific Conference Series, p. 591

Iaria R., Di Salvo T., Robba N.R., et al., 2005a, ApJ634, L161

Iaria R., Di Salvo T., Robba N.R., et al., 2005b, ApJ634, L161

Jahoda K., Markwardt C.B., Radeva Y., et al., 2006, ApJS163, 401

Janka H.T., 2012, Annual Review of Nuclear and Particle Science 62, 407

Johnson W.R., Soff G., 1985, Atomic Data and Nuclear Data Tables 33, 405

Kelley R.L., Mitsuda K., Allen C.A., et al., 2007, PASJ59, 77

Kompaneets A.S., 1957, Soviet Journal of Experimental and Theoretical Physics 4, 730

Koyama K., Tsunemi H., Dotani T., et al., 2007, PASJ59, 23

Krause M.O., Oliver J.H., 1979, Journal of Physical and Chemical Reference Data 8, 329

Krimm H.A., Barthelmy S.D., Markwardt C.B., et al., 2006, In: AAS/High Energy Astrophysics Division #9. AAS/High Energy Astrophysics Division, p. 13.47

Kühnel M., Fürst F., Pottschmidt K., et al., 2017a, A&A607, A88

Kühnel M., Fürst F., Pottschmidt K., et al., 2017b, A&A607, A88

Lamb F.K., Pethick C.J., Pines D., 1973, ApJ184, 271

Latal H.G., 1986, ApJ309, 372

Leahy D., Igna C., 2012, In: Petre R., Mitsuda K., Angelini L. (eds.) American Institute of Physics Conference Series, Vol. 1427. American Institute of Physics Conference Series, p.306

Longair M.S., 2011, High Energy Astrophysics

Lucas P.W., Hoare M.G., Longmore A., et al., 2008, Monthly Notices of the Royal Astronomical Society 391, 136

Malacaria C., Klochkov D., Santangelo A., Staubert R., 2015, Astronomy and Astrophysics 581, A121

Marcu D.M., Pottschmidt K., Gottlieb A.M., et al., 2015, arXiv e-prints arXiv:1502.03437

Martin R.G., Nixon C., Armitage P.J., et al., 2014, ApJ790, L34

Mewe R., Gronenschild E.H.B.M., van den Oord G.H.J., 1985, A&AS62, 197

Mitsuda K., Bautz M., Inoue H., et al., 2007, PASJ59, S1

Müller S., Ferrigno C., Kühnel M., et al., 2013, A&A551, A6

Nagase F., Corbet R.H.D., Day C.S.R., et al., 1992, ApJ396, 147

Naik S., Paul B., Ali Z., 2011, The Astrophysical Journal 737, 79

Okajima T., Soong Y., Balsamo E.R., et al., 2016, Space Telescopes and Instrumentation 2016: Ultraviolet to Gamma Ray 9905, 99054X

Petterson J.A., 1978, ApJ224, 625

Pierrard V., Lopez Rosson G., Borremans K., et al., 2014, Space Sci. Rev.184, 87

Postnov K.A., Gornostaev M.I., Klochkov D., et al., 2015, Monthly Notices of the Royal Astronomical Society 452, 1601

Prigozhin G., Gendreau K., Doty J.P., et al., 2016, Edinburgh, United Kingdom, p. 99051I

Reig P., Milonaki F., 2016, Astronomy and Astrophysics 594, A45

Roming P.W.A., Kennedy T.E., Mason K.O., et al., 2005, Space Sci. Rev.120, 95

Ruiter A.J., Ferrario L., Belczynski K., et al., 2019, Monthly Notices of the Royal Astronomical Society 484, 698

Saio H., Nomoto K., 1985, Astronomy and Astrophysics 150, L21

Sako M., Liedahl D.A., Kahn S.M., Paerels F., 1999, ApJ525, 921

Schandl S., Meyer F., 1994, Astronomy and Astrophysics 289, 149

Schreier E., Levinson R., Gursky H., et al., 1972, ApJ172, L79

Schreier E.J., Swartz K., Giacconi R., et al., 1976, The Astrophysical Journal 204, 539

Schwarm F.W., Schönherr G., Falkner S., et al., 2017, A&A597, A3

Schönherr G., Wilms J., Kretschmar P., et al., 2007, Astronomy and Astrophysics 472, 353

Smartt S.J., 2009, Ann. Rev. A&A47, 63

Sootome T., Nakajima M., Mihara T., et al., 2011, The Astronomer's Telegram 3829, 1

Suchy S., Pottschmidt K., Wilms J., et al., 2008, ApJ675, 1487

Suchy S., Pottschmidt K., Wilms J., et al., 2008, The Astrophysical Journal 675, 1487

Sukhbold T., Ertl T., Woosley S.E., et al., 2016, ApJ821, 38

Takahashi T., Abe K., Endo M., et al., 2007, PASJ59, 35

Tanaka Y., 1986, Observations of Compact X-Ray Sources, Vol. 255, p. 198

Tauris T.M., Sanyal D., Yoon S.C., Langer N., 2013, A&A558, A39

Thompson T.W.J., Rothschild R.E., 2009, ApJ691, 1744

Thébault E., Finlay C.C., Beggan C.D., et al., 2015, Earth, Planets and Space 67, 79

Tjemkes S.A., Zuiderwijk E.J., van Paradijs J., 1986, A&A154, 77

Truemper J., Pietsch W., Reppin C., et al., 1978, ApJ219, L105

West B.F., Wolfram K.D., Becker P.A., 2017, The Astrophysical Journal 835, 130

Wojdowski P.S., Liedahl D.A., Sako M., et al., 2003, The Astrophysical Journal 582, 959

Wolff M.T., Becker P.A., Gottlieb A.M., et al., 2016, ApJ831, 194

Wolff M.T., Becker P.A., Gottlieb A.M., et al., 2016, The Astrophysical Journal 831, 194

Acknowledgements

This thesis would not have been possible without the generous support of numerous people. First and foremost I want to thank Jörn Wilms for giving me the opportunity to work at the beautiful Dr. Remeis Observatory, for always being supportive and giving valuable advise whenever needed. I also want to especially thank Ralf Ballhausen, who I could always go to and annoy with my questions. Further, I want to acknowledge the support by Katja Pottschmidt and the whole *NICER* team for providing fascinating insight in the workings of their satellite and for their work to provide the scientific community with the full potential of this unique instrument. For her extremely valuable aid concerning emission line physics, I want to thank Natalie Hell, whose helpfulness really stood out to me. Besides the already named, the whole Remeis "family" deserves my wholehearted gratitude, for making the observatory such a welcoming and pleasant place to work at. Last, but not least, I want mention my parents, whose moral and caloric support I would not want to miss.

Declaration of Authorship

I hereby certify that the thesis I am submitting is entirely my own original work except where otherwise indicated. I am aware of the University's regulations concerning plagiarism, including those regulations concerning disciplinary actions that may result from plagiarism. Any use of the works of any other author, in any form, is properly acknowledged at their point of use.